Mars

Article *in* The Astronomy and Astrophysics Review · March 1998

3 authors, including:

Mars

Tilman Spohn, Frank Sohl, and Doris Breuer

Institut für Planetologie, Westfälische Wilhelms–Universität Münster, Wilhelm-Klemm-Str. 10,
D–48149 Münster, Germany

Abstract. Mars is the fourth planet out from the sun. It is a terrestrial planet with a density suggesting a composition roughly similar to that of the Earth. Its orbital period is 687 days, its orbital eccentricity is 0.093 and its rotational period is about 24 hours. Mars has two small moons of asteroidal shapes and sizes (about 11 and 6 km mean radius), the bigger of which, Phobos, orbits with decreasing semimajor orbit axis. The decrease of the orbit is caused by the dissipation of tidal energy in the Martian mantle. The other satellite, Deimos, orbits close to the synchronous position where the rotation period of a planet equals the orbital period of its satellite and has hardly evolved with time. Mars has a tenous atmosphere composed mostly of CO_2 with strong winds and with large scale aeolian transport of surface material during dust storms and in sublimation-condensation cycles between the polar caps. The planet has a small magnetic field, probably not generated by dynamo action in the core but possibly due to remnant magnetization of crustal rock acquired earlier from a stronger magnetic field generated by a now dead core dynamo. A dynamo powered by thermal power alone would have ceased a few billions of years ago as the core cooled to an extent that it became stably stratified. Mars' topography and its gravity field are dominated by the Tharsis bulge, a huge dome of volcanic origin. Tharsis was the major center of volcanic activity, a second center is Elysium about $100°$ in longitude away. The Tharsis bulge is a major contributor to the non-hydrostaticity of the planet's figure. The moment of inertia factor together with the mass and the radius presently is the most useful constraint for geophysical models of the Martian interior. It has recently been determined by Doppler range measurements to the Mars Pathfinder Lander to be 0.3662 ± 0.0017 (Folkner et al. 1997). In addition, models of the interior structure use the chemistry of the SNC meteorites which are widely believed to have originated on Mars. According to the models, Mars is a differentiated planet with a 100 to 200 km thick basaltic crust, a metallic core with a radius of approximately half the planetary radius, and a silicate mantle. Mantle dynamics is essential in forming the elements of the surface tectonics. Models of mantle convection find that the pressure-induced phase transformations of α-olivine to β-spinel, β-spinel to γ-spinel, and γ-spinel to perovskite play major roles in the evolution of mantle flow fields and mantle temperature. It is not very likely that the γ-spinel to perovskite transition is present

Correspondence to: T. Spohn (e-mail: spohn@uni-muenster.de) Institut für Planetologie, Westfälische
Wilhelms-Universität, Wilhelm-Klemm-Str. 10, D–48149 Münster, Germany

in Mars today, but a few 100 km thick layer of perovskite may have been present in the lower mantle immediately above the core-mantle boundary early in the Martian history when mantle temperatures were hotter than today. The phase transitions act to reduce the number of upwellings to a few major plumes which is consistent with the bipolar distribution of volcanic centers of Mars. The phase transitions also cause a partial layering of the lower mantle which keeps the lower mantle and the core from extensive cooling over the past aeons. A relatively hot, fluid core is the most widely accepted explanation for the present lack of a self-generated magnetic field. Growth of an inner core which requires sub-liquidus temperatures in the core would have provided an efficient mechanism to power a dynamo up to the present day.

Keywords. Mars, Evolution, Interior, Dynamics, Tectonics, Satellites

1. Introduction

The planet Mars is of particular interest to the public as its environmental conditions are the most earthlike of any of the terrestrial planets. Today, Mars is a desert planet with strong winds and regularly occuring dust storms in a thin carbon dioxide rich atmosphere characterizing the environment. The surface temperature is nearly habitable. It varies between 140 K at night in winter and 300 K at midday in summer. In the past, Mars most probably had a much denser, warmer, and wetter atmosphere as outflow channels, river beds, and now dried out lakes suggest. It has even been speculated that the northern hemisphere may have been covered by an ocean. The surface temperature and the evidence for water in its early history suggest that primitive life forms may have formed on the planet. Recent findings (Wright et al. 1989, McKay et al. 1996, Grady et al. 1996) of possible traces of life in meteorites widely believed to come from Mars have reconfirmed the public interest.

To the interested scientist, Mars offers an even wider variety of interesting questions to study, in particular, as an object of comparative planetology. Mars' overall density is inbetween those of the high density metal and silicate rich inner earthlike planets and the low density gaseous outer planets. Its present location and with some probability its place of formation is close to the well where Jupiter's gravity caused a minimum in the surface density of mass. The differences in present atmospheric compositions between the Earth and Mars are interesting to atmosphere evolution modelers as well as the substantial differences in pressure and temperature between the atmospheres of Venus and Mars which are chemically quite similar. It is at present still unknown whereto the water has been lost. But it is possible that a significant part if not most of it is still on Mars as permafrost in the regolith and in the polar caps.

Surface landforms on Mars vary significantly from regions of sandy deserts to volcanic plains to heavily cratered areas. On a global scale, the surface is characterized by what is known as the Martian dichotomy: The northern hemisphere is covered by diverse plains, lava flows and sedimentary deposits and showing a relatively small crater density. The latter suggests that the surface there is relatively young and has been altered by endogenic volcanic activity through the Martian history, possibly up to the geologically recent past (a few 100 Ma ago). It has been speculated that lava may still extrude at the floor of Valles Marineris, a giant graben structure on Tharsis (Lucchitta 1987). The southern hemisphere is characterized by heavily cratered terrain and is comparatively old wearing the signs of the post-accretional bombardment when the planets swept up most of the debris left over from the formation of the solar system
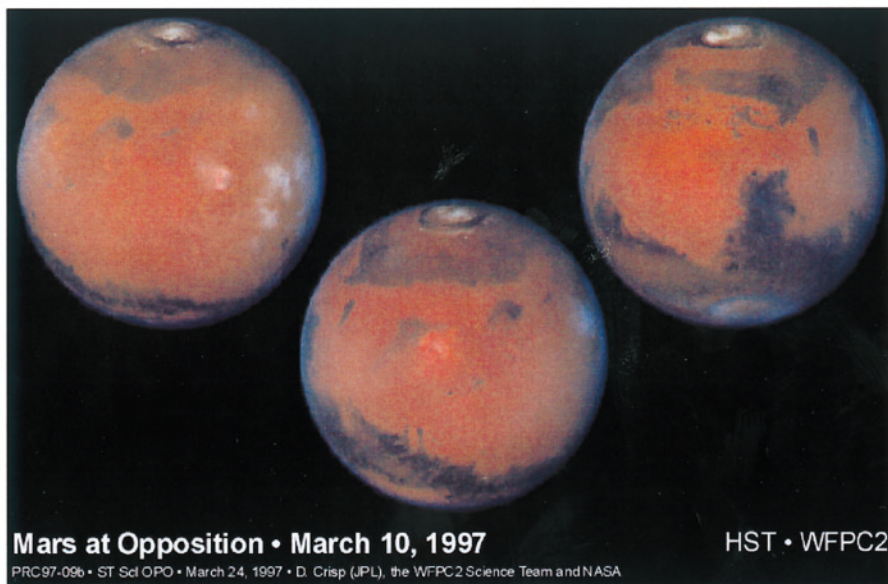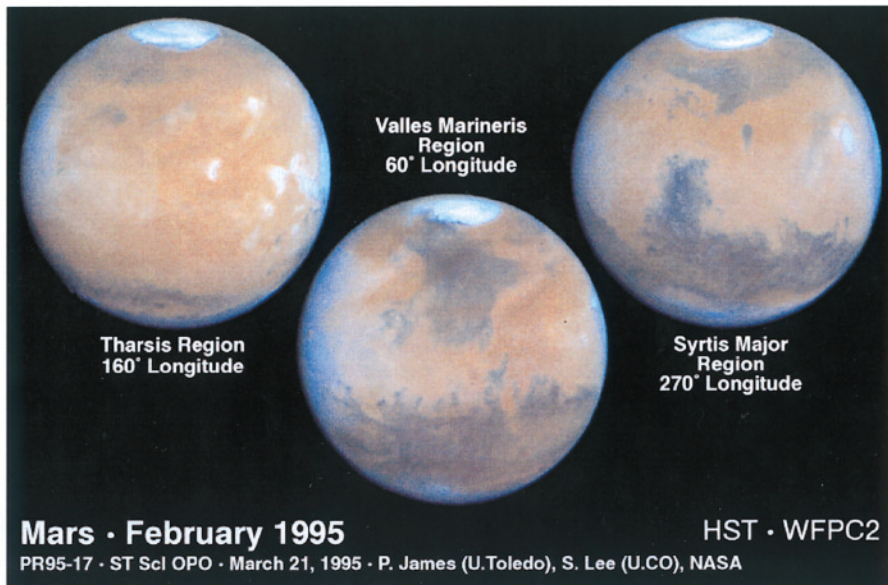
Fig. 1. Global views of Mars during spring in the northern hemisphere (top images) and one day before northern summer solstice (bottom images). North is at the top and east is to the right. The true color images were taken through three different color filters with the Wide Field Planetary Camera 2 aboard NASA's Hubble Space Telescope at two subsequent oppositions, when Mars was at a distance of about 100 million kilometers from Earth. While Hubble's recently refurbished Planetary Camera resolved Martian surface features at a scale of 22 km at central longitudes near 160, 210, and 305 degrees at opposition in 1997, image resolution was 50 km at central longitudes near 160, 60, and 270 degrees at opposition in 1995. Much of the bright north polar carbon dioxide frost cap has sublimated during spring, so that the much smaller permanent water ice cap surrounded with dark sand dunes becomes visible at summer solstice. Water vapor in the atmosphere freezes out to form ice-crystal clouds downwind from the giant volcanos on the Tharsis Plateau (east of center on left-hand images) and in the Elysium region (east of center on upper right-hand image and center on lower middle image), and in the giant impact basin Hellas (near bottom of right-hand images). Hubble makes it possible to monitor seasonal changes of bright and dark Martian albedo provinces over a couple of years with an image resolution comparable to that of Earth's weather satellites (© *NASA/JPL/STScI*)

in its early history. There are a few large impact basins in the southern hemisphere, the most prominent of which is the Hellas basin, but these are not comparable in size relative to the planetary radius with the mare basins on the Moon. Global views of Mars which were recently taken with the Hubble Space Telescope are shown in Fig. 1.

A recent reanalysis of spacecraft occultation data and Earth bound radar topographic profiles suggests that the hemispheric dichotomy of Mars is caused by an offset of about 3 km between the planet's center-of-mass and center-of-figure. The boundary between the two hemispheres which is characterized by outflow channels and chaotic terrain forms on a regional scale appears to consist of broad gradual slopes along most of its length rather than several kilometers high scarps (Smith and Zuber 1996). Near the boundary but more in the northern hemisphere the giant Tharsis dome is located. Tharsis features three enormous volcanoes that together with the even bigger volcano Olympus Mons located somewhat more to the North East form the most prominent volcanic center on Mars that may have been active up to the geologically recent past. The volcanoes are shield volcanoes similar to their counterparts on Earth such as Hawaii but are much larger in scale, a fact that can be explained by the differences in surface gravity between the two planets. A second center, Elysium, is located almost 100° to the West. A further but much older and more eroded volcanic structure, Alba Patera, is also found near Tharsis. Although these volcanoes are impressive, by far the greatest volume of volcanic material was emplaced as vast flood lavas (Greeley and Spudis 1981). The dominance of the two volcanic centers, in particular Tharsis, and their apparent age and long time activity suggests that convection in the underlying mantle is more stable as compared with convection in the mantles of Earth and Venus and is dominated by a small number of large upwelling plumes.

Mars' interior structure is similar to that of the other terrestrial planets. There is an iron-rich core of approximately half the planet radius, a silicate mantle and a basaltic crust. The size of the core and the thickness of the crust are at present weakly constrained by the gravity field and the chemistry of meteorites believed to come from Mars. The state of the core is unknown and is a matter discussed in thermal evolution models of the planet. The mantle is convecting, thereby removing heat from the interior and powering the endogenic activity. While this is similar to what is happening on other terrestrial planets and satellites, the differences in size and mass are likely to cause differences in interior dynamics and evolution. A major difference between the Earth and Mars is found in global tectonic style: While the Earth features plate-tectonics, Mars like most others has an immobile rigid outer shell or lithosphere penetrated by volcanic vents. However, it has been speculated that Mars also once had plate tectonics that ceased aeons ago (Sleep 1994).

A further interesting global characteristic of Mars is the absence of a significant present magnetic field. In that Mars is similar to Venus and the Moon which also lack self-sustained magnetic fields but different from Earth and Mercury and different, as the recent data from the Galileo spacecraft suggests, from the Jovian moon Ganymede (Kivelson et al. 1996b) and, possibly, Io (Kivelson et al. 1996a). A comparison between these bodies suggests that size and rotation rate are not the primary parameters determining the presence of a dynamo in the interior of a terrestrial planetary body. Rather, the generation of the magnetic field may depend on the size and present state of the iron rich core.

Planetary science is a very diverse and interdisciplinary field with contributions from Earth sciences as well as physics, chemistry and biology. In the present review we attempt to show the broad variety of questions raised for Mars but we will be

biased to some extent towards Martian geophysics and geology. In particular, we will address the interior structure of Mars, the dynamics of its mantle and its thermal and tectonic evolution and will attempt to demonstrate how these elements fit together and depend on each other. Mars science has been reviewed in a number of publications but it is evolving at a relatively fast pace. For the most extensive and complete recent review we refer the reader to Kieffer et al. (1992).

Table 1. Global Properties of Mars

	Value
Semimajor axis, AU	1.52366
Eccentricity e	0.0934
Inclination i, deg	1.8504
Mean daily motion n_{orb}, deg d^{-1}	0.52405
Mean orbital velocity v_{orb}, km s^{-1}	24.13
Period of revolution $\tau_{\rm rev}$, s	5.92314×10^7
Period of rotation $\tau_{\rm rot}$, s	8.86427×10^4
Obliquity ψ, deg	25.2
Planetocentric constant	
$\quad GM_p$, m^3 s^{-2}	4.28283×10^{13}
Global mass M_p, kg	6.41850×10^{23}
Mean surface radius r_p, km	3389.92
Mean compressed density $\bar{\rho}$, kg m^{-3}	3933.5 ± 0.4
Surface gravity g_p, m s^{-2}	3.727
Mean escape velocity v_{esc}, m s^{-1}	5.027
Dimensionless polar moment	
$\quad$ of inertia factor $C/M_p r_p^2$	0.3662 ± 0.0017
Gravitational oblateness J_2	1960.454×10^{-6}
Center of mass/center of figure offset d, km	2.5 ± 0.07
Magnetic dipole moment M_B, T m^3	$< 8 \times 10^{11}$
Mean specific dissipation factor	
$\quad$ estimate Q_p	50–150
Surface pressure p_p, Pa	560
Surface temperature T_p, K	210
Surface bolometric albedo A_{bol}	0.08–0.4
Mean atmospheric scale height h_e, km	10.8
Period of main Phobos	
$\quad$ tide $\tau_{\rm tid}$, s	1.992×10^4

References: Smith and Born (1976), Thomas (1991), Kieffer et al. (1992), and Yoder and Standish (1997)

2. General Survey: Mars as a Solar System Body

In this section, we will review the present knowledge about Mars as a terrestrial planet. In Table 1 we have collected parameter values that characterize the planet. We will start with reviewing its orbit and rotational dynamics and discuss the figure, the gravity field, the magnetic field, the mineralogy of the surface and the interior, the geology and the tectonics, the atmosphere, and the satellites. Our knowledge stems mostly from the results of space missions, in particular from the results of the *Mariner*, the *Viking*, and the *Phobos* missions. However, it is believed that we do have samples of Martian origin in our laboratories. These meteorites named SNC meteorites after their finding places Shergotty, Nakhla, and Chassigny are supplemented by ALH84001 and have been of immense value for Mars science.
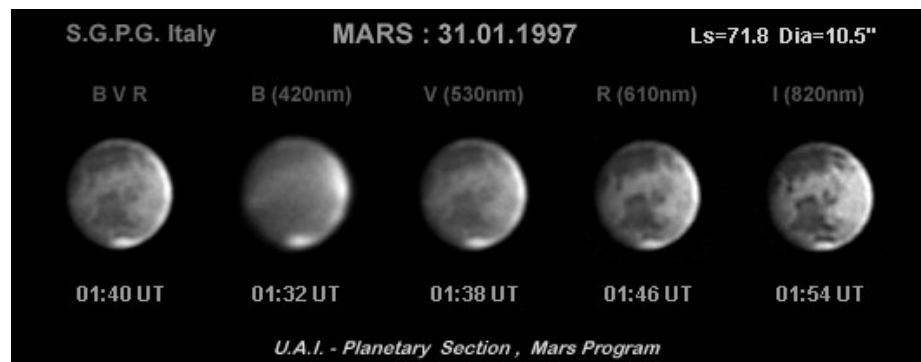
Fig. 2. Image sequence of Mars midway between aphelion and northern summer solstice acquired on January 31, 1997, using the Marco Falorni Planetary Observatory's ISIS CCD-800 camera and 30 cm Cassegrain reflector at direct focus (F/24). Each monochrome CCD-image is the enhanced sum of four normalized original frames taken in blue (centered at 420 nm), green (centered at 530 nm), red (centered at 610 nm) and infrared (centered at 820 nm) colored filters. The outer left image results from a combination of the blue-, green-, and red-colored filter images. South is at the top. The images show the bright polar cap and dark Mare Acidalium in the northern hemisphere, while the dark markings in the southern hemisphere represent Mare Erythraeum, Sinus Aurorae, Sinus Margariter, and Sinus Meridiani (© *San Gersole Planetary Group*)

Orbit and Rotation Dynamics

Mars, our outer neighbour planet, requires 687 days to complete one revolution about the sun. The mean opposition interval, the time that elapses between subsequent closest encounters with Earth, is 780 days. Because of Mars' comparatively large orbital eccentricity of $e = 0.093$, the distance between Earth and Mars at the time of a rare perihelic opposition is about half the distance during the more frequent aphelic oppositions. The apparent diameter of Mars as seen from Earth therefore varies between about $3''.5$ at aphelic conjunction, $13''.8$ at aphelic opposition, and $25''.1$ at perihelic opposition. Mars is a rapid rotator. The rotation period is $24^{h}\ 37^{m}\ 22^{s}.6$, quite similar to that of the Earth but much smaller than those of Venus and Mercury. The rotation period varies by up to ± 0.04 s over a Martian year as a consequence of moment of inertia variations caused by seasonal variations in the ice coverage of the polar caps (Davies et al. 1992, Esposito et al. 1992). The rotation axis is inclined by $25.1894 \pm 0.0001°$ with respect to the planet's orbital plane, and the north pole points to a region intermediate between the constellations Cepheus and Cygnus ($\alpha_0 = 317°.341$ in right ascension and $\delta_0 = 52°.711$ in declination). The above value of the obliquity has been determined at a midpoint in the *Viking* epoch (January 1, 1980) from *Viking* lander range data by Yoder and Standish (1997). The mean precession rate of the rotation axis was determined from the same data set to be -7.83 ± 0.30 arc sec a^{-1}. Because of this particular orientation of the rotational axis, the southern hemisphere is directed towards Earth during perihelion, whereas the northern hemisphere is best visible from Earth during aphelion. Figure 2 shows telescopic images of Mars recently obtained by the San Gersole Planetary Group operating the Marco Falorni Planetary Observatory near Florence, Italy.

Due to the inclination of the rotation axis and the fact that the solar insolation during perihelion is by a factor of $((1+e)/(1-e))^2$ larger than that during aphelion,

the surface and the atmosphere of Mars experience considerable seasonal variations resulting in varying sizes of the polar ice caps and changes in the global pattern of dark surface albedo markings caused by seasonal dust storms. The history of the obliquity has drawn considerable interest (see Ward (1992) for a review). The dynamic coupling of the evolution of the obliquity to the precession of the normal to the orbital plane and to the inclination and eccentricity of the orbit may have caused the obliquity to evolve significantly over the past eons with important consequences for the history of the Martian climate since the solar insolation is a strong function of the obliquity. Model calculations suggest excursions of the obliquity up to values of $45°$ as little as 5 Ma ago. For the present obliquity the solar flux varies by roughly a factor of two between the poles and the equator. For an obliquity of $45°$ the solar flux is approximately constant over the surface during daytime.

Geodesy and Gravity

The fundamental geodetic parameters mass, radius, and the oblatenesses of the figure and the gravity field are required to constrain models of the Martian interior. Prior to the 1960s, before space probes were sent to Mars for the very first time, estimates of the planet's mass and radius were solely based on telescopic observations using micrometric and photographic techniques. The extremely disturbing influence of the Martian atmosphere on telescopic measurements of the optical or geometrical flattening caused by the planet's rapid rotation resulted in significant overestimates of the mean equatorial radius a in comparison with the relatively accurate determinations of the polar radius c (Urey 1952, Esposito et al. 1992). The dynamical flattening $(C - A)/C$, where C and A are the polar and mean equatorial moments of inertia was determined from observations of the retrograde precession of the orbits of the two small Martian satellites Phobos and Deimos. The dynamical flattening is a consequence of the rotationally induced oblateness of the planet's gravity field. It was shown with the early data that the dynamical flattening is significantly smaller than the geometrical flattening of the planet (Wells 1979) indicating non-hydrostaticity of the planet's figure. Mass M_p was determined from the orbital elements of Phobos and Deimos. While their periods of revolution were known with sufficient accuracy, estimates of the planetocentric constant GM_p, where G is the universal gravitational constant, suffered primarily from inaccurate determinations of the satellite orbit axes.

The value of the planetocentric constant $GM_p = 42\,900 \pm 70$ km^3 s^{-2} of Mars as determined by Asaph Hall in 1878 from the orbital movements of Phobos and Deimos was improved by operating two-way radio Doppler instruments during the very successful *Mariner*– and *Viking* missions. During the close flyby of *Mariner 4* in 1965, a value of $GM_p = 42\,828.32 \pm 0.13$ km^3 s^{-2} was determined, which is in excellent agreement with $GM_p = 42\,828.36 \pm 0.05$ km^3 s^{-2}, the most recent value obtained from a joint inversion of *Mariner 9*– and *Viking*–Doppler data (Smith et al. 1993). The accepted value of the mean radius r_p of 3389.92 ± 0.04 km was obtained by using earth-bound radar observations and radio occultation data from the *Mariner 9*– spacecraft that went into orbit around Mars in 1972 (Bills and Ferrari 1978). Using the generally accepted value of 6.4185×10^{23} kg for the total mass of Mars, the mean compressed density is 3933.5 ± 0.4 kg m^{-3}, where the error is primarily due to uncertainties in the value of the gravitational constant G (Esposito et al. 1992). This value of the density is inbetween those for the Moon and for the Earth.

The Martian gravity field was surveyed with two-way radio Doppler tracking of the *Mariner 9* orbiter in 1971 – 1972 and the *Viking* orbiters during 1976 – 1979 (Sjogren et al. 1975, Christensen and Balmino 1979, Balmino et al. 1982, Smith et al. 1993). The technique uses the Doppler effect on radio signals transmitted from the Earth to the spacecraft and back. The frequency shift of the radio signals returned by the spaceprobe relative to the signal emitted from the ground station is proportional to the velocity component along the direction of vision or line of sight and allows the calculation of the line-of-sight (LOS) acceleration of the spaceprobe. These data can then be used to calculate the gravity field at a resolution determined by the frequency of signal transmission to the spacecraft. Gravity anomalies can be interpreted in terms of chemically or thermally induced lateral and depth variations of density. However, it should be noted that these interpretations suffer from non-uniqueness problems inherent in any inversion of the gravity field.

The topography of the Martian surface has been measured basically using two different remote sensing techniques from orbiters. Radio occultation of the spacecraft by Mars has been used to directly determine the radius. Spectral remote sensing data collected by ultraviolet spectrometers and infrared radiometers and stereophotogrammetric interpretations of images taken from slightly different positions in orbit have been used to measure topography on a finer scale. More indirect estimates of the large-scale topography of the surface use the correlation between relative variations in topography and atmospheric Rayleigh scattering in the ultraviolet light as well as the strength of CO_2-induced absorption bands in the infrared. These observations are supplemented by earth-bound radar altimetric data. In particular during perihelion oppositions, high-resolution topographic profiles of the equatorial regions have been constructed thereby considerably improving topographic control networks (Davies et al. 1992). Radar altimetry from spacecraft has not yet been done on Mars. A radar altimeter was part of the payloads of the lost *Mars Observer* and *Mars96* missions. The latter missions would have allowed the calculation of a digital elevation model with unprecedented accuracy using laser altimeter and the stereo capabilities of the two stereo cameras from DLR, Germany. A radar altimeter is part of the payload of *Mars Global Surveyor* which is on its way to Mars at the time of this writing.

The spherical harmonic representation of the long-wavelength part of the Martian gravity potential at locations exterior to the planet is given by the superposition of the gravitational potential Φ_g and the rotational potential Φ_{rot} according to

$$
\begin{aligned}
\Phi^0(r, \lambda, \varphi) &= \Phi_g + \Phi_{rot} \\
&= -\frac{GM_p}{r} \left\{ 1 - \sum_{n=2}^{\infty} \left(\frac{a}{r}\right)^n J_n \mathrm{P}_n(\sin\varphi) \right. \\
&\quad + \sum_{n=2}^{\infty} \sum_{m=1}^{n} \left(\frac{a}{r}\right)^n \left(C_{n,m}\cos m\lambda + S_{n,m}\sin m\lambda\right) \mathrm{P}_n^m(\sin\varphi) \\
&\quad \left. + \frac{1}{3}\frac{\omega^2 r^3}{GM_p}\left(1 - \mathrm{P}_2(\sin\varphi)\right) \right\},
\end{aligned}
\tag{1}
$$

where GM_p is the planetocentric constant and $\omega = 2\pi/\tau_{rot}$ is the rotation rate. (r, λ, φ) denote radial distance from the center-of-mass and areocentric longitude and latitude, respectively. P_n and P_n^m are the zonal and the associated Legendre polynomials of degree n and order m. Hence, the zonal contributions to the gravitational potential

Φ_g are represented by the multipole moments $J_n = -C_{n,0}$, while the harmonic coefficients $C_{n,m}$ and $S_{n,m}$ represent sectorial ($n = m$) and tesseral ($n \neq m$) contributions to the potential caused by deviations from a rotationally symmetric mass distribution (e.g., Wells 1979). Annual solar tides and, on shorter timescales, tides raised by Phobos and Deimos cause displacements of mass in the interior. The gravity potential and the large-scale topography are superimposed by these additional periodic disturbances which are proportional to the external tidal disturbance potential Φ_2^e.

The frequency content of the amplitude spectrum of the gravitational potential

$$\sigma_n(\Phi^0, \Phi^0) = \left[\frac{1}{2n+1} \sum_{m=0}^{n} (\bar{C}_{n,m}^2 + \bar{S}_{n,m}^2) \right]^{\frac{1}{2}} \approx \frac{A}{n^2} \tag{2}$$

calculated from the fully normalized harmonic coefficients

$$(\bar{C}_{n,m}, \bar{S}_{n,m}) = \left[\frac{(n+m)!}{(2 - \delta_{0,m})(2n+1)(n-m)!} \right]^{\frac{1}{2}} (C_{n,m}, S_{n,m})$$

with $\bar{J}_n = -\bar{C}_{n,0}$ allows some important insight into the rheology and the mechanical and thermal properties of the lithosphere, the outer rigid shell of the planet. The value of the empirically determined constant of proportionality A for $n < 15$ is found to be approximately 10^{-5} for the Earth's gravity field (Kaula 1968). Planets of smaller size and surface gravity which should cool faster due to the larger ratio between surface area and volume are expected to show comparatively rough gravity fields (Janle and Meissner 1986). Using Doppler data from the *Viking* mission it was shown that (2) is well approximated by the empirical relation

$$\sigma_n = \frac{1.3 \times 10^{-4}}{n^2} \tag{3}$$

for the gravitational field of Mars. The roughness of the 610 Pa–areoid thus exceeds that of the Earth's geoid by about one order of magnitude as expected.

Analogous to (1), the variation of the radial distance of the surface r_s from the planet's center of figure caused by the large-scale topography can be expanded into spherical harmonics to give

$$r_s(\lambda, \varphi) = r_p \left\{ 1 - \sum_{n=1}^{\infty} \left(\frac{2n+1}{3} \right) T_n \mathrm{P}_n(\sin \varphi) \right.$$
$$\left. + \sum_{n=1}^{\infty} \sum_{m=1}^{n} \left(\frac{2n+1}{3} \right) \left(A_{n,m} \cos m\lambda + B_{n,m} \sin m\lambda \right) \mathrm{P}_n^m(\sin \varphi) \right\} \tag{4}$$

with $T_n = -A_{n,0}$ the zonal and $A_{n,m}$ and $B_{n,m}$ the sectorial ($n = m$) and tesseral ($n \neq m$) harmonic coefficients. The mean surface radius r_p of Mars is a topographic datum based on a niveau spheroid of degree and order $n_{max} = m_{max} = 4$ which provides the best approximation to the 610 Pa isobar. The latter is the pressure of the H_2O–triple point in the Martian atmosphere (Christensen 1975).

Early spherical harmonic representations of the gravity potential subsequent to the *Mariner 9* mission provided the first detailed estimates of the low harmonic coefficients from which the oblateness of the Martian gravity field was confirmed and the

orientation of the rotational axis improved (Esposito et al. 1992). Spherical harmonic expansions were calculated with harmonic coefficients $(C_{n,m}, S_{n,m})$ of maximum degree and order $n_{max} = m_{max} = 6$ (Reasenberg et al. 1975) and $n_{max} = m_{max} = 9$ (Sjogren et al. 1975). The global distribution of the areoid heights relative to the niveau spheroid given by the quadrupole moment $J_2 = -C_{2,0}$ and the harmonic coefficients $C_{2,1}$ and $S_{2,1}$ were shown to be given by

$$J_{2,2} = (C_{2,2} + S_{2,2})^{\frac{1}{2}}. \tag{5}$$

This showed that the gravity potential of Mars is characterized by a pronounced equatorial ellipticity which is caused by the Tharsis Rise. A less pronounced elevation of the 610 Pa–areoid is located above Isidis Planitia close to the volcanic highland plane Syrtis Major Planitia which is located almost diametrically away from the Tharsis Rise. There is thus a significant correlation between the long-wavelength part of the 610 Pa–areoid and the large-scale topography of the Martian surface (Reasenberg et al. 1975, Sjogren et al. 1975).

Early spherical harmonic models of the surface topography based on *Mariner 9* radio occultation data, spectral data, and radar altimetric data were based on harmonic coefficients $(A_{n,m}, B_{n,m})$ of maximum degree and order $n_{max} = m_{max} = 8$. The relatively large contributions of the low harmonic coefficients of degrees $n = 1$ and $n = 2$ indicate an hemispheric asymmetry of the Martian surface and require an offset of the center-of-mass of the planet relative to its center-of-figure by about 2 km. The topographic relief varies by up to 32 km in relative height, measured from the base of the Hellas impact bassin to the summit of the shield volcano Olympus Mons (Christensen 1975). As a consequence, the hypsographic curve for the Martian surface features three maxima of different width and height. These represent the highly-cratered southern highlands, the volcanic northern lowlands, and the giant impact basins of the southern hemisphere (e.g., Meissner 1986). By using an improved inversion method, Bills and Ferrari (1978) extended the spherical harmonic representation of the topography to degree and order $n_{max} = m_{max} = 16$. The improved values of the dipole moment $T_1 = -A_{1,0}$ and the first harmonic coefficients $A_{1,1}$ and $B_{1,1}$ were interpreted in terms of a center-of-mass/center-of-figure offset of 2.50 ± 0.07 km shifted along areocentric coordinates $\varphi = 62\overset{\circ}{.}0 \pm 3\overset{\circ}{.}7$ S and $\lambda = 87\overset{\circ}{.}7 \pm 3\overset{\circ}{.}0$ W (Esposito et al. 1992).

With the availability of Doppler data from the two *Viking* orbiters the spherical harmonic representation of the gravitational potential was extended to terms $(C_{n,m}, S_{n,m})$ of maximum degree and order $n_{max} = m_{max} = 12$ (Christensen and Balmino 1979) and later to $n_{max} = m_{max} = 18$ (Balmino et al. 1982). The positive correlation of the 610 Pa–areoid with the topographic mass distribution became significantly more apparent with the better data and the long-wavelength areoid anomalies above Tharsis Planitia, Hellas Planitia and Isidis Planitia were confirmed (Fig. 3). Because Doppler data of sufficient accuracy are not available to date for the southern polar latitudes, the zonal harmonic coefficients $J_n = -C_{n,0}$ were determined only up to degree $n = 10$.

The strong negative correlation of the topography with the distribution of the Bouguer–gravity (gravity corrected for contributions of topographic masses above the reference aeroid) anomalies for harmonic degrees $4 \leq n \leq 10$ suggests that the large-scale topography of the Martian surface, except for the huge shields of the volcanic provinces Tharsis and Elysium, is to a large extent isostatically compensated (Christensen and Balmino 1979, Balmino et al. 1982). Stress compensation in these regions is expected to occur at a mean depth of 100 to 200 km beneath which
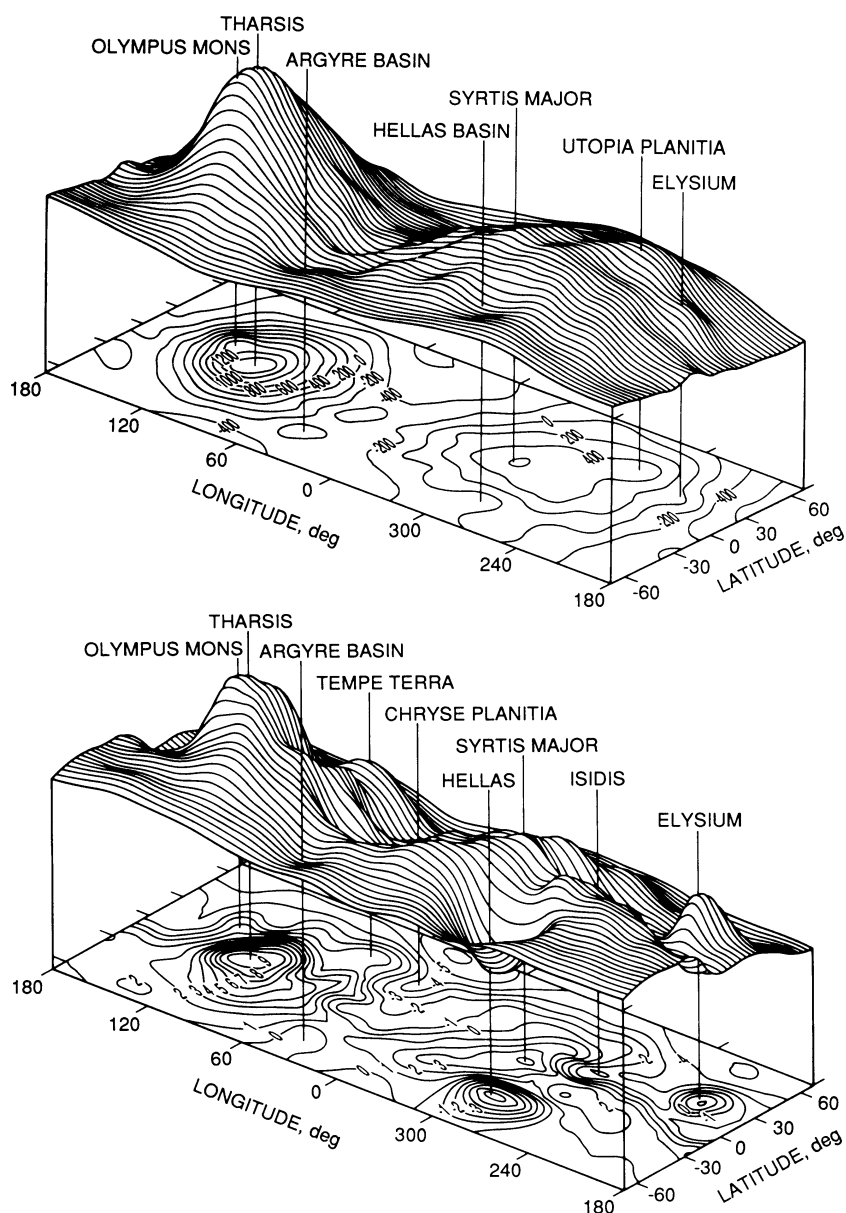
Fig. 3. Mercator projections of the non-hydrostatic part of the areoid (top) and the large scale topography of Mars (bottom) deduced from spherical harmonic representations of maximum order and degree $n = m = 16$. The contour line interval is 200 m in case of the areoid, whereas the separation of topography contours is 1 km. The field is dominated by the Tharsis high and shows a good correlation with major topographic features such as the Tharsis and Elysium volcanoes, Olympus Mons, the Hellas basin, and Isidis Planitia. Volcanic structures such as Olympus Mons, Elysium Mons, the Tharsis Montes, Alba Patera (an ancient widely eroded shield volcano), and Utopia Patera are typically associated with gravity highs. The giant impact basin Hellas Planitia and the Valles Marineris feature gravity lows. Isidis Planitia, also a large impact structure, has a gravity high at its center and gravity lows near its edges (Esposito et al. 1992; figure reprinted from Fig. 10, page 231 and Fig. 11, page 232, from Gravity and Topography. In H.H. Kieffer, B.M. Jakosky, C.W. Snyder, and M.S. Matthews, editors, *Mars*, pages 209–248, Univ. of Ariz. Press, Tucson; © 1992 by The University of Arizona Press)

the planet should be in approximate hydrostatic equilibrium. This depth could be the depth to the crust-mantle boundary (Esposito et al. 1992). The prominent gravity anomaly above the Tharsis Rise for $n = 2$ and $n = 3$, however, would imply unrealistically large compensation depths of 1100 km and 600 km, respectively. An alternative, probably dynamic compensation mechanism is required, if compressional tectonics by horizontal stresses is assumed to be absent (Phillips and Saunders 1975, Phillips and Lambeck 1980).

Recently, a reanalysis of almost the entire set of two-way Doppler data was done by Smith et al. (1993) in preparation of the *Mars Observer* mission and an improved spherical harmonic model of the gravitational potential termed *Goddard Mars Model 1* (GMM-1) was calculated. The model uses the inverse relation between the spectral amplitude and the square of the harmonic degree n^2 to extend the harmonic expansion to terms $(C_{n,m}, S_{n,m})$ of maximum degree and order $n_{max} = m_{max} = 50$. This corresponds to a spatial resolution of 200 to 300 km. As a result, it was shown that the well known correlation between the long-wavelength contributions to the 610 Pa–areoid and the large-scale topography of the Martian surface exists even for regional features such as single volcanic shields, impact basins, and tectonic grabens. However, the planetwide geopotential topography (topography relative to the aeroid) offset of about 2 to 3 km between the northern and southern hemispheres is not reflected in the free-air gravity anomaly field. The two hemispheres may be isostatically compensated on a large scale by crustal thickness differences (Smith et al. 1993). Older interpretations of the Martian figure suggested that the southern hemisphere is a highland with respect to the northern hemisphere and with a topographic offset of 1 to 3 km (e.g., Carr 1986). A recent reanalysis of occultation data from the *Mariner 9* and *Viking* Orbiter spacecraft to determine the shape of Mars (Smith and Zuber 1996) has shown that the figure of the planet does not show the expected depression in the north. Rather the apparent topographic difference reflects the 3 km center-of-mass center-of-figure offset.

Magnetic Field

Magnetic field data in the vicinity of Mars have been gathered by a number of space missions, most recently by the Russian *Phobos* mission in 1989. The strength of the interplanetary magnetic field frozen in the solar wind is about 3 nT at Mars and the inclination of the field is 53° with respect to the Mars–sun line. In general, the magnetic field near Mars can be described in terms of a magnetic potential Φ_B that is given in spherical harmonics by (e.g., Connerney 1993)

$$\Phi_B(r, \lambda, \varphi) = a \sum_{n=1}^{\infty} \left\{ \left(\frac{a}{r}\right)^{n+1} T_n^i + \left(\frac{r}{a}\right)^n T_n^e \right\} \tag{6}$$

with

$$T_n^i = \sum_{m=1}^{n} \left(g_{n,m} \cos m\lambda + h_{n,m} \sin m\lambda \right) \mathrm{P}_n^m(\sin \varphi)$$

and

$$T_n^e = \sum_{m=1}^{n} \left(G_{n,m} \cos m\lambda + H_{n,m} \sin m\lambda \right) \mathrm{P}_n^m(\sin \varphi)$$
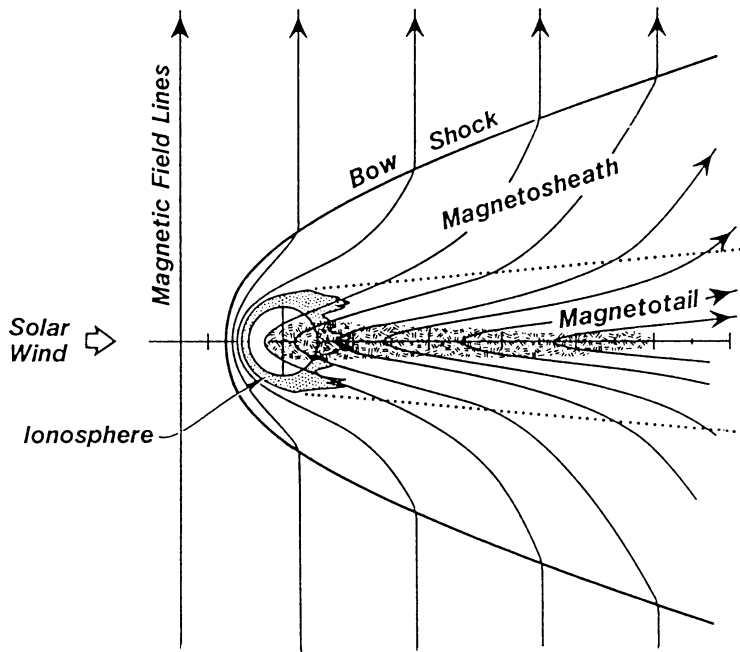
Fig. 4. Interaction of the solar wind and the frozen-in interplanetary magnetic field with the Martian ionosphere. The polarity distribution of the induced magnetotail is controlled by draped interplanetary magnetic field lines piled up in the magnetosheath (Luhmann and Brace 1991, figure reprinted from Fig. 10, page 127, from Near-Mars Space. *Rev. Geophys.*, **29**, 121–140, © 1991 by the American Geophysical Union)

The first term in curly brackets in (6), a series in inverse powers of radius r normalized to the equatorial radius a, represents the potential of the internally generated field. The second term represents contributions due to external sources. $(g_{n,m}, h_{n,m})$ and $(G_{n,m}, H_{n,m})$ are the corresponding internal and external Gaussian coefficients which are analogous to the zonal, sectorial, and tesseral harmonic coefficients of the gravity and topography fields in (1) and (4). The moment and orientation of an internally generated magnetic dipole are then determined by the three coefficients g_{10}, g_{11}, and h_{11}.

The spacecraft data show a bow shock and a magnetosheath indicating that Mars provides an obstacle to the solar wind that is somewhat larger than the size of the planet. The formation of a hyperbolical bow shock at the sunward side of the planet is caused by the deceleration of the solar wind plasma flow from supersonic velocities of about 400 km s^{-1} to much lower subsonic values. In the magnetosheath's turbulent flow regime subsequent to the bow shock (Fig. 4), the interplanetary magnetic field interacts with the Martian ionosphere with alternating compressions and extensions of magnetic field lines and variable but substantial heating of intruding solar wind plasma (Luhmann and Brace 1991, Russell 1993). The bow shock was observed by particle and fields experiments on the various spacecrafts that flew to Mars. The shock data are usually fit to a conic section curve with

$$R = \frac{R_T}{1 + e_{bs} \cos \theta} \tag{7}$$

where R is the radial distance to the shock from the center of Mars, R_T is radius of the shock at the terminator (the day-night boundary), e_{bs} is the eccentricity of the conic section, and θ is the solar zenith angle, the angle between the Mars–sun line and the point of interest. The form and the size of the bow shock vary with solar wind strength but it was found that the subsolar distance is only 1.5 planetary radii. This compares with a subsolar distance of the Earth's bow shock of 13 planetary radii and with that of Venus (a planet lacking a magnetic field) of about 1.2 planetary radii. These data suggest that if Mars had an intrinsic magnetic field, it would be weak.

Some of the missions also discovered a magnetosheath but it was concluded from modeling (Russell et al. 1984) that the magnetic field lines piled up in the magnetosheath could be explained as consisting of draped solar wind fields. The *Phobos* observations added unambiguous magnetotail data. There is evidence from the spacecraft's high-resolution magnetometer experiments in the planet's equatorial plane, that the magnetic polarity of the magnetotail beyond the orbit of the Martian satellite Phobos is basically determined by the interplanetary magnetic field (Riedler et al. 1989). This finding would be consistent with a Martian magnetic moment

$$M_B = a^3 \sqrt{g_{10}^2 + g_{11}^2 + h_{11}^2} \tag{8}$$

of less than 1.5×10^{12} T m^3 (Luhmann et al. 1992, Russell 1993). Estimates of the magnetic dipole moment have decreased and become more accurate over the past decades and have settled to a value of about 2×10^{-4} times the Earth's present magnetic moment of 7×10^{15} T m^3. This field may be induced or generated by a weak dynamo in the interior. An alternative possibility has been discussed in a number of publications, most recently by Leweling and Spohn (1997). In these models the field is due to a remanently magnetized crust which was magnetized by an early dynamo that ceased to exist a few billion years ago. This assumption is supported by the remnant magnetization of some of the SNC meteorites. In particular, the data from the Shergotty meteorite (Cisowski 1986) suggests that Mars may have had a magnetic field with a dipole moment of 10^{13} T m^3 only 1.3 Ga ago.

The apparent absence of a dynamo driven magnetic field at the present time, in spite of Mars' appreciable core size and rapid rotation, has often been contended to indicate either a solid state of the core or a completely molten core devoid of intrinsic heat sources necessary to drive sufficiently vigorous thermal convection. Recent thermal history calculations by Schubert and Spohn (1990) suggest that the latter would require an initial core sulfur content of about 15 wt.% or more. For smaller initial sulfur concentrations, an inner core would freeze out and the continuous release of latent heat and gravitational energy would be sufficient to drive a dynamo with a substantial field at present. It has also been suggested, however, that the shielding effect of the iron–rich Martian mantle and the reduced electric conductivity of a sulfur-rich core alloy could frustrate the operation of a self-sustained dynamo (Anderson 1972).

Composition and Mineralogy

A rough estimate of the mineralogical composition of rock on the Martian surface can be obtained from spectroscopy in the optical wavelength range between 0.3 μm and

50 μm. However, there is convincing evidence that about one dozen achondritic meteorites known to date and collectively termed SNCs (Shergotty, Nakhla, Chassigny) are igneous crustal rocks from Mars. The parent rocks of these meteorites most probably were generated by partial melting in the uppermost mantle and emplaced in the crust by volcanic activity. There they remained mostly unaltered by weathering processes until they were accelerated by one or several impacts to the Martian escape velocity of 5 km s^{-1}. This must have happened about 180 Ma ago as their cosmic ray exposure ages suggest (Jagoutz 1991).

The best arguments for the Martian origin of the SNC meteorites stem from their comparatively young crystallisation ages of 0.15 to 1.3 Ga (Jagoutz 1991), from their mineralogy that requires parent magma formation at pressures representative of the uppermost Martian mantle, and from atmospheric gas inclusions in impact glasses of one shergottite. The chemistry of the gas resembles the composition of the Martian atmosphere as measured by the *Vikings*. The basaltic shergottites contain dense, polymorphous plagiclase-, olivine-, and pyroxen varieties that resulted from shock metamorphism whereas the augit- and pigeonit-rich Nakhlites and the olivine-rich Chassigny meteorites have apparently not been shock metamorphized (McSween 1985, 1987). Because of their comparatively young crystallisation ages and basaltic to ultramafic compositions, the SNC meteorites are believed to have been expelled from relatively young terrain in the northern lowlands. The Tharsis Province has recently been suggested to represent the most probable surface area for potential SNC parent craters (Mouginis-Mark et al. 1992). There is petrographic and isotopic evidence that the comparatively old, orthopyroxenite meteorite ALH84001 is closely related to the SNC meteorites (Mittlefehldt 1994). Of course, the age of ALH84001 weakens one of the arguments for the SNCs originating from Mars. ALH84001 presumably represents old igneous crustal rock ejected during a separate impact on the southern hemisphere (Treiman 1995, Ash et al. 1996). The SNCs as well as ALH84001 are characteristically depleted in volatile, moderately volatile, and siderophile-chalcophile elements (e.g., Wänke 1991).

It is commonly assumed that the bulk composition of the terrestrial planets is chondritic. Evidence for a chondritic bulk composition is provided by the abundances of condensable elements in carbonaceous chondrites of petrologic type 1 (C1) which agree well with those in the solar photosphere. This is particularly true for the refractory elements such as the lanthanides and the main rock forming elements Si, Ti, Mg, Al, Ca (Taylor 1988). The global Fe/Si ratio for carbonaceous chondrites is 1.71. Carbonaceous chondrites are believed to represent the most primitive material in the solar system (Wänke and Dreibus 1988, Wasson and Kallemeyn 1988). Possible deviations from a chondritic bulk composition of a planet may have been caused by early fractionation of lithophile, refractory and moderately volatile elements in the solar nebula before the onset of accretion. Additional metal-silicate fractionation subsequent to core formation in the young planet may have occurred as a consequence of mantle rock spall off by impact-induced blasts during the late heavy bombardment in the inner solar system. These mega-impact events are generally believed to be less important for Mars, but may have been of utmost importance for Mercury and Moon (Taylor 1988).

An estimate of the bulk composition of a terrestrial planet from crustal rock is possible by correlating pairs of incompatible elements in rock samples. Because the concentrations of these elements are not altered by magmatic processes, their abundance ratios are taken to be representative of the whole planet (Wänke 1981). Refractory, incompatible elements such as U and La in SNC meteorites show C1
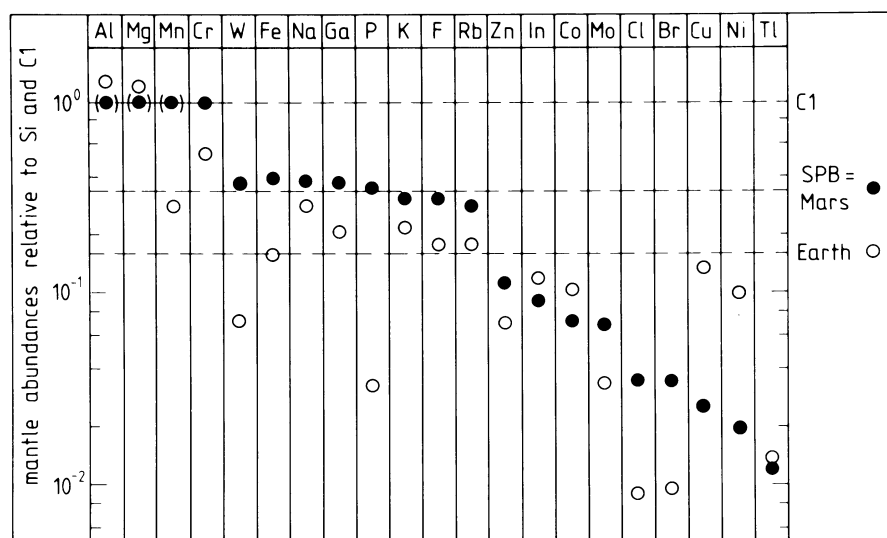
Fig. 5. Comparison of estimated major and trace element abundances in the mantles of Mars and Earth with respect to silicium and a C1 standard chondrite. In accordance with thermal equilibrium condensation models of the solar nebula, the analysis of SNC meteorites suggests a two to three times larger content of volatile and moderately volatile elements for the Martian mantle as compared to that of the Earth. Furthermore, the siderophile-chalcophile elements are found to be much more depleted in the Martian mantle than in the terrestrial mantle (Wänke 1991 figure reprinted with kind permission from Kluwer Academic Publishers from Fig. 3, page 5, from Chemistry, accretion, and evolution of Mars. *Space Sci. Rev.*, **56**, 1–8, © 1991 by Kluwer Academic Publishers)

abundance ratios, which is taken as evidence for a C1 chondritic bulk composition, albeit one that is depleted in volatiles. The correlation of moderately volatile, incompatible elements such as K and Rb, however, indicates the presence during accretion of an additional more oxidized component containing volatiles in C1 abundances. From this and similar observations, the two component accretion model for Earth and Mars was derived by Ringwood (1979) and Wänke (1981). Judging from the concentration of moderately volatile elements in SNC meteorites, the mass fraction of the volatile rich component is estimated to have been 30 to 40% (Fig. 5). This component may represent primordial, C1 chondritic material that originated in the asteroid belt, whereas the reduced, volatile-free component is believed to have come from the hotter, inner regions of the solar nebula (Dreibus and Wänke 1985, 1987, Wänke and Dreibus 1988, Wänke 1991).

The Martian mantle must have experienced extensive early degassing and hydrogen escape following the equilibration of water with metallic iron in the presence of the volatile rich component. Equilibration of water with iron during core formation resulted in a comparatively dry silicate mantle highly oxidized and particularly rich in FeO. The accretion scenario offers an explanation for the FeO–rich compositions of the SNC magma source regions and, thereby, for the geologic evidence for several hundreds of kilometers long lava flows. The lava must have had an extremely low viscosity that may be explained by its FeO–rich composition. (McGetchin and Smyth 1978, McSween 1985). The H_2O content of the present man-

tle has been determined to be 36 ppm, equivalent to a planetwide ocean of 130 m depth (Wänke and Dreibus 1988, Wänke 1991). In terms of the major volatile–free minerals, the upper mantle has been concluded to contain about 50 wt.% olivine, 30 wt.% low–calcium orthopyroxene, 20 wt.% high–calcium clinopyroxene and minor aluminous phases such as low–pressure plagioclase. The latter are replaced one after the other by spinel and garnet with increasing depth (Longhi et al. 1992). Most of the sulfur from the oxidized, volatile-rich component is assumed to have formed a sulfur-rich metallic alloy from the surplus Fe and Ni present in the nebula. The depletion of chalcophile elements is then understood to be a consequence of metallic alloy segregation during early core formation. It has been proposed that considerable amounts of hydrogen might have been dissolved in the iron phase. The hydrogen would reduce the density and melting temperature of the Martian core far beyond that which would be expected for a sulfur–rich Fe-Ni-FeS core (Zharkov et al. 1991).

The Martian surface, except for the strongly variable polar regions, can roughly be subdivided into two albedo provinces with respect to its brightness, color, and spectral properties. There are bright, orange regions of high red albedo (~ 0.4) and dark regions of differing colors and low red albedo (~ 0.1). There is no pronounced brightness contrast in blue light since the blue albedo is about 0.05 for each region (Soderblom 1992). Very dark red regions can be identified with the ancient southern highlands while the bright regions correlate with the young northern lowlands although there are prominent dark patches caused by sand dunes and sheets in the northern hemisphere. The strong brightness contrast in red light is subject to considerable seasonal variations due to annual planet-wide duststorm activity. Large-scale dust storm activity causes the redistribution of fine-grained materials on a regional or even global scale thereby regularly providing transient coverage of the dark albedo provinces (Soderblom 1992, Singer and McSween, Jr. 1993). In contrast, the aeolian transport of dark materials appears to occur on a more local scale indicative of less modified, coarse materials locally derived from dark bedrock.

The broadest absorption bands with the largest effect on color perception by the human eye occur in the short-wavelength range and are due to the exchange of charges in crystals containing Fe^{3+}-ions. These materials seem to constitute a major part of the dark and bright albedo regions. The observations indicate that the oxidation state of the fine-grained, bright materials is generally higher than that of the coarse-grained, dark materials. The reflectivities of the bright albedo provinces are similar to that of terrestrial basalts modified by extensive weathering processes through hydrothermal alteration (palagonitisation). Currently, iron-rich palagonites may offer the best explanation for reflection and transmission spectra obtained by remote sensing in the thermal infrared. From these spectral observations, the quartz content of the atmospheric dust has been determined to be about 60%, which suggests an intermediate-type basalt as parent material (Soderblom 1992).

Singer and McSeen, Jr. (1993) emphasize that the achondritic meteorite Shergotty, a nominal example representing the basaltic shergottite group among the SNC meteorites, reveals the same spectral characteristic in the pyroxen bands (λ 1.0 μm and λ 2.0 μm) as the dark, geologically old albedo provinces close to the equator. Furthermore, the shapes and locations of the pyroxene bands suggest, that the coarse-grained, less-oxidized material of the dark albedo provinces representing Mars' old highland crust provinces may have originated from an almost unmodified basaltic crust. Since Shergotty is a comparatively young magmatic crustal rock, this observation suggests that the composition of the Martian crust is entirely basaltic and similar to that of the Shergottites, independent of the age of single crustal provinces. The
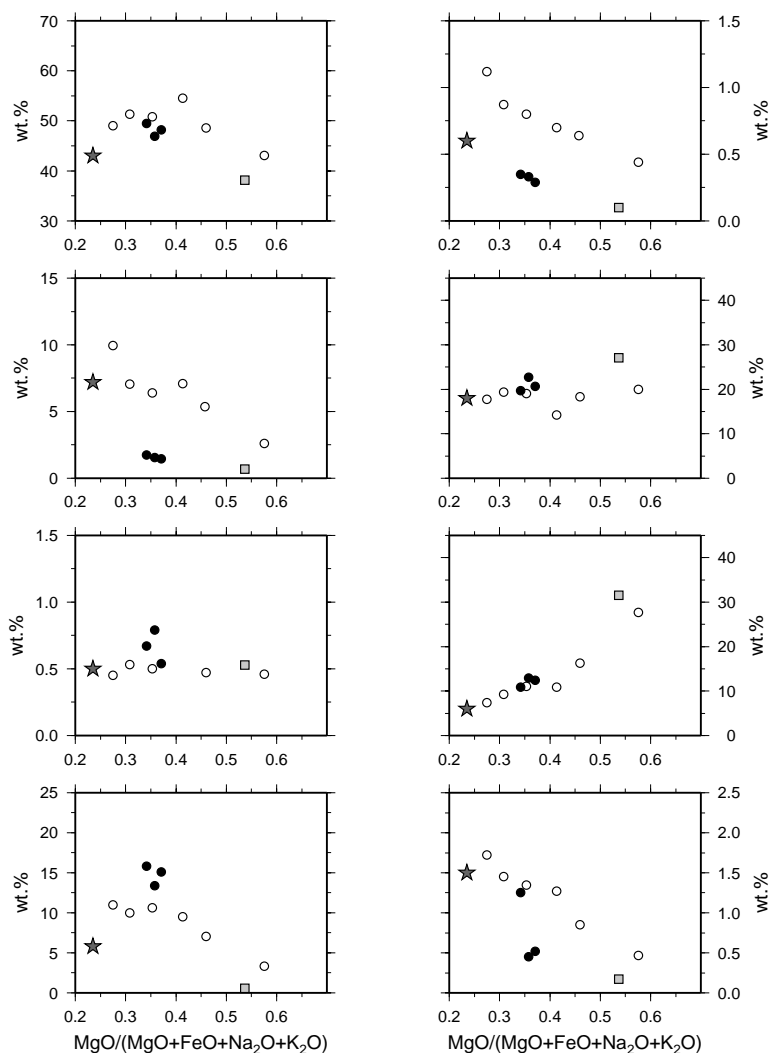
Fig. 6. Element correlations among SNC meteorites. Oxide abundances in basaltic shergottites (open circles), pyroxene-rich nakhlites (solid circles), and Chassigny, an olivine-rich dunite (quadrangle), are given in wt.% as a function of their mafic and moderately volatile portions represented by the solidification index $MgO/(MgO+FeO+Na_2O+K_2O)$. The particularly close match to linear correlations among the shergottites suggests that the average soil composition at the Viking landing sites (filled asterisks) is quite similar to that of the shergottites

crustal age provinces appear to differ mostly with respect to the oxidation state of the crust (Singer and McSween, Jr. 1993).

The two *Viking* landers carried out *in-situ* –X-ray fluorescence measurements of the bright, fine-grained material in the transition region between bright and dark albedo provinces. Although both landing sites are several thousand kilometers apart and although samples were collected from depths greater than 0.25 m, the analyses were found to be nearly identical at both sites. Accordingly, the bright surface ma-

terial is enriched in iron and reveals low concentrations of Al, Rb, Sr, Y, Zr and a reduced K/Ca–ratio. This composition is similar to that of the shergottites (Fig. 6) The relatively high content of S and Cl as sulfates and chlorites in the *Viking* samples probably results from the early formation of a cementation horizon of regional extent (*duricrust*) (Banin et al. 1992, Stoker et al. 1993). The small difference between the two surface analyses suggests an intensive regolith mixture over a period of several hundred million years. Regolith mixture by planet-wide dust storm activity occurs on a considerably shorter timescale than erosional processes on the Martian surface. Because of the elevated erosional activity in the old, cratered highlands in the past, most of the bright material may represent advanced weathering products derived from coarse, eroded debris that have been originally supplied by the southern highland crust thereby dominating regolith composition. Thus, the composition of the bright material is expected to be representative of the chemical composition of the Martian crust. It appears to consist primarily of basaltic rock and there appear to be no granitic or anorthositic crustal provinces (Taylor 1992).

Geology and Tectonics

The major geologic division of Mars' surface is known as the crustal dichotomy: there is a distinct hemispheric asymmetry in the distribution of its geologic units (Fig. 7). The southern hemisphere is densely cratered and therefore older than the sparsely cratered northern hemisphere. The boundary between the two hemispheres is characterized by knobby and fretted terrain and by detached plateaus distributed over a width of about 700 km (Sharp 1973, Carr 1981, Wilhelms and Squyres 1984). The northern hemisphere was probably resurfaced by volcanic activity early in the Martian history (e.g., Carr 1981) and may have been the site of an early ocean (Baker et al. 1991). Channels in the boundary region between the hemispheres have been identified as former rivers and stream valleys where a large amount of water must have flowed. It is possible that these flows occurred repeatedly and were not isolated events. The boundary region has also been suggested to be the site of relic plate boundaries (Sleep 1994). A recent reanalysis of occultation data from the *Mariner 9* and *Viking* Orbiter spacecraft to determine the shape of Mars (Smith and Zuber 1996) has shown that the figure of the planet does not show the expected depression in the north. A depression shows in the geopotential topography which is the topography relative to the aeroid. Thus the water has flown from regions of high geopotential in the south to regions of low geopotential in the north. Aditional interpretation of earth-bound radar data (Smith and Zuber 1996) has shown that the boundary between the hemispheres along most of its length consists of broad gradual slopes over distances of thousands of kilometers.

The cause of the hemispheric asymmetry is unknown. Some planetary scientists propose that the dichotomy is a result of a giant impact (Wilhelms and Squyres 1984) or several impact events (Frey et al. 1988). Others (Wise et al. 1979, McGill and Dimitriou 1990, e.g.,) suggest endogenic causes related to mantle dynamics. In any case, it is likely that the dichotomy formed already in the early history of Mars during or at the end of the heavy bombardment. This early bombardment is recorded in the ancient southern crust and it has been suggested that this part of the crust was formed until around 3.8 Ga ago. The more sparsely cratered surfaces would be of younger ages. The Martian stratigraphy has been divided into three distinct chronostratigraphic units: the Noachian, Hesperian and Amazonian Systems (e.g.,
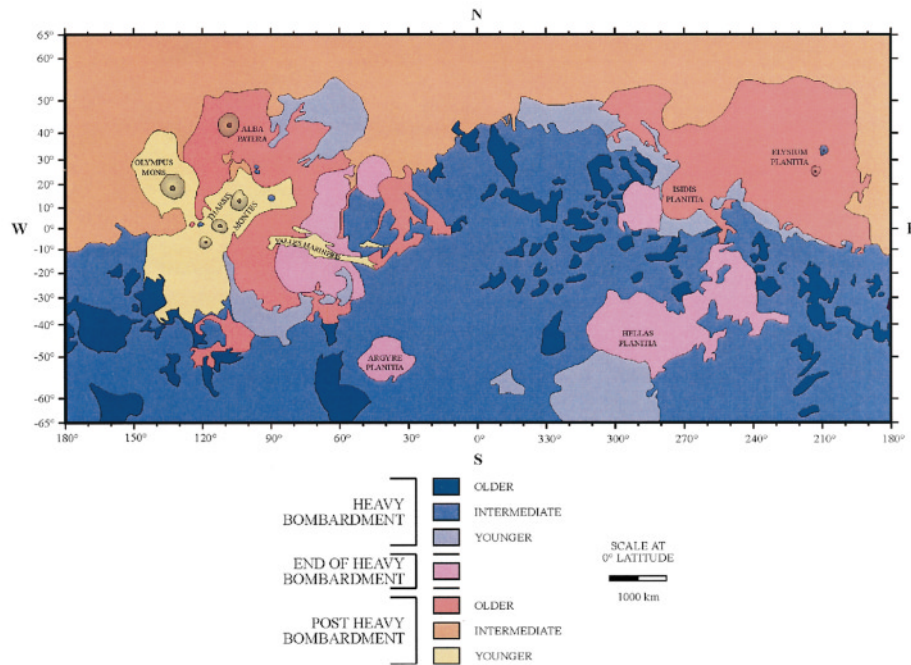
Fig. 7. Geological map of Mars. North is at the top and east is to the right. The ages of Martian surface units are assigned relative to the end of the late heavy bombardment. The formation of red, orange and yellow areas took place after the period of late heavy bombardment whereto the blue areas refer. The origin of the Martian crustal dichotomy between the young, sparsely cratered northern hemisphere and the old, densely cratered southern hemisphere is basically unknown (figure modified after Kieffer et al. 1992)

Tanaka 1986). These are based on rock sequences and represent the major periods of geologic activity. Since direct measurements of absolute ages are unavailable at the present time, model ages have been calculated using crater density-age relations established for the Moon and correcting for differences in impactor fluxes between the Moon and Mars. But these ages vary widely among existing models (Neukum and Wise 1976, Hartmann et al. 1981).

The old southern hemisphere of Mars superficially resembles the highlands of the Moon, but there are differences. Most of the Martian craters have been strongly eroded by wind and water, and the floor of many of the larger craters have been filled with sediments. In addition, the craters are often fractured, and crossed by abundant small channels. This valley network has been formed early, probably by subsurface water that reached the surface through small springs (Baker et al. 1992). Areas between some of the craters are also blanketed with windblown dust, or covered with lava flows. Another striking feature of the Martian impact craters is the flowlike pattern of the impact ejecta. The distinctive pattern may result from the interaction of the ejecta with the atmosphere (Schultz and Gault 1979, Schultz 1986), or, as the preferred explanation, the ejecta materials were saturated with water by the ground containing water or ice (Carr et al. 1977).

The relatively young northern hemiphere is covered with diverse plains which include large areas of lavas and sedimentary deposits. The most striking geological

and tectonic features such as the huge volcanoes and the Valles Marineris canyon are located there. The Tharsis dome, a broad, elevated area centered on the equator at 105° W with the three Tharsis volcanoes Ascraeus Mons, Arsia Mons, and Pavonis Mons is located just north of the dichotomy boundary. Valles Marineris cuts into the Tharsis dome near the Martian equator. Together with Olympus Mons which is located just off the northwestern edge of the Tharsis region Tharsis forms the major of two volcanic centers on Mars. The other one, Elysium, centered at 25° N, 210° W lies approximately 100° in longitude away from Tharsis. To the north of Tharsis is located the ancient and large but substantially eroded shield volcano Alba Patera. These volcanoes are enormous by terrestrial standards, with Olympus Mons the biggest shield volcano in the solar system standing more than 24 km above its surroundings. Despite the young surfaces of the Tharsis and Elysium volcanoes they may actually be quite old. Volcanism in the Tharsis region apparently, as the geologic record suggests, continued for a period of over 3 Ga up to the recent past (Neukum and Hiller 1981). The comparatively large size of the volcanoes probably results from a combination of the relative small value of gravity, lack of plate tectonics, and long-term stability of mantle convection.

Valles Marineris is a vast system of canyons that extends about 4000 km eastward. The canyons appear to have formed largely by faulting. However, the valley system has also been enlarged by wind and water erosions and parts of it are filled with sediments (Lucchitta et al. 1992). Other, smaller tectonic features have disrupted thousands of km^2 extending radially away from the Tharsis bulge. Approximately a third of the planet's surface has been affected by these processes. These fractures probably formed in response to the huge load that the bulge's immense mass forms.

Mars' young polar regions are distinctively different from the rest of the planet. Layered deposits presumed to be composed of CO_2, water ice, and dust occur at both poles. At the south polar area the deposits extend outward to about the 80° latitude circle. In the north, the layered deposits are surrounded by a vast array of sand dunes. During local summer CO_2 sublimes into the atmosphere there, whereas in the local winter time the atmospheric carbon dioxide again freezes out onto the polar regions. The changes of the polar regions between summer and winter as well as the fact that the surface is mainly modified by wind or aeolian processes shows the essential role of the interaction between the surface and the atmosphere.

Atmosphere

The atmosphere of Mars is essentially a pure carbon dioxide atmosphere that contains various minor constituents including water vapor, carbon monoxide, atomic oxygen, ozone, and atomic hydrogen. The surface pressure is less than one hundredth of the pressure at the surface of the Earth. It varies considerably with location due to elevation differences and with the seasons due to condensation and sublimation of CO_2 on the polar caps. The southern polar cap dominates the pressure cycle; its winter is longer and colder than at the north pole and, therefore, incorporates a correspondingly larger volume of atmospheric CO_2 during southern winter.

The seasonal conditions at the polar caps together with the surface temperature also control the amount of water vapor in the atmosphere. Extensive cloud systems appear on Mars and perhaps all those that have been observed are composed of ice crystals. Because of the thinness of the atmosphere and the lack of oceans with high thermal inertia, the temperature varies by about 50° C from day to night. The

lowest temperatures at the surface of the planet are at the winter pole, limited by the condensation to be near the frost point of carbon dioxide (148 K at 600 Pa pressure). The highest surface temperatures are located near the equator and can reach 320 K. However, the vertical temperature gradient near the surface is very steep and 1 to 2 m above the ground the temperature is already substantially lower. An important effect on the atmospheric and surface temperature is due to a constant dust haze extending from the surface up to 50 km in height. This dust haze is changing its density depending on the global and local style of the atmospheric circulation, thereby substantially influencing the albedo of the atmosphere.

The atmospheric circulation of the planet is controlled mainly by radiative forcing and by Coriolis forces, modified by the surface topography and albedo variations. The absence of large bodies of liquid water simplifies the circulation pattern in contrast to that of the Earth. The exchange of carbon dioxide between the atmosphere and the polar caps plays an important part in the climate system and is probably related to the observed spectacular global dust storms appearing in some years. More local storms with velocities of about 25 m s^{-1} are likely the results of the topography and albedo variations. This is much more pronounced on Mars as compared to Venus and Earth because of the thin atmosphere and its more rapid response to local ground temperature variations.

The early history of the atmosphere is poorly understood. For instance how much volatile material Mars has outgassed over the ages, how much escaped to space thermally or as a result of an impact, and how much remains either frozen or chemically converted is basically unknown. The present low pressure and low temperature do not allow the presence of liquid water on the planet. In areas where the surface warms up to temperatures above the freezing point ice transforms directly into water vapor. However, if the evidence from orbital imagery of abundant water on the surface in the past is accepted (e.g., McCauley et al. 1972), the surface temperature and pressure must have been sufficiently higher at earlier times. In view of its current cold climate and a lower solar luminosity (faint-young-sun paradox) several billion years ago, a strong greenhouse effect must be postulated for the early evolution (e.g., Walker 1978). A likely greenhouse gas is CO_2 because it is already known to be present in the atmosphere today and is not rapidly broken down by sunlight. An atmospheric presence of CO_2 on early Mars equivalent to 5×10^5 Pa (five times the Earth's current surface pressure) would warm the surface above the freezing point (Pollack et al. 1987). The loss of CO_2 from the atmosphere may have occurred partly by outgassing into space and partly by absorption in near-surface reservoirs. Major sinks for CO_2 might have been the reversible absorption into the regolith and the irreversible formation of carbonate rocks. This hypothesis has the problem, however, that the strong greenhouse effect caused by the large amounts of CO_2 would have been reduced rapidly by an enhanced rate of absorption into the regolith and carbonate rock formation at times when liquid water was available. These processes are so efficient and rapid that it is hard to find a scenario in which a CO_2 atmosphere could survive even to 3.8 Ga ago. The presence of other greenhouse gases might help but they are broken down very easily by the sunlight. A further question remains as to what happened to the proposed large amount of water. It is commonly concluded, that a significant quantity of water still resides on Mars, probably locked up beneath the surface as ground ice. The regolith is also a possible reservoir for CO_2. Its pore volume is substantial, and a large amount of this volume can be expected to be at temperatures cold enough for CO_2 ice to be present (Squyres et al. 1992).
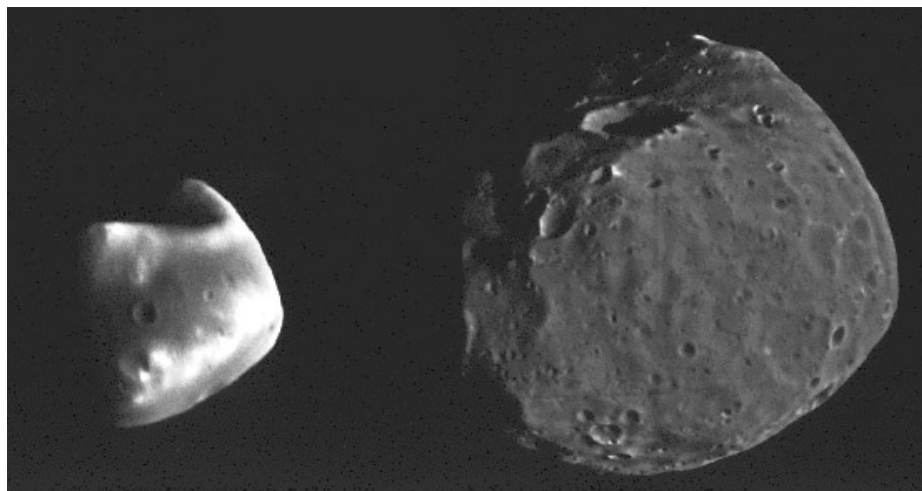
Fig. 8. Comparison of the Martian satellites Phobos (right) and Deimos (left). Both satellites are heavily cratered and much darker than most inner asteroid belt satellites. Ejecta blocks and downslope movements of surface materials are present on both satellites. However, the surfaces of Phobos and Deimos differ from each other in that Phobos features well-preserved craters and linear depressions while Deimos is covered by subdued craters filled with debris. Their spectral properties are similar to those of dark, carbonaceous C-type outer belt asteroids at 2.8 to 3.3 AU distance from the Sun (© *NASA/JPL*)

Satellites

The two Martian satellites are irregularly shaped bodies with rugged limb profiles that indicate fragmentation by impact processes. The largest well-defined craters on their surfaces are comparable to the sizes of the satellites themselves (Fig. 8). Their surfaces are best approximated by triaxial ellipsoids with the largest principal axes pointing within a few degrees in the direction of Mars and spin axes perpendicular to their orbital planes. Both satellites are rotationally locked into a 1:1 spin-orbit coupling. Small deviations from perfect synchronization arise from geometrical librations in longitude of the sub-Mars point amounting to twice the orbit eccentricities and from forced rotational librations induced by the satellites' irregular shapes. The mean ellipsoidal radii are $13.3 \times 11.1 \times 9.3 \pm 0.3$ km for Phobos and $7.5 \times 6.2 \times 5.4 \pm 0.5$ km for Deimos. Variations of topographic elevations with respect to the ellipsoids are of the order of 1 km (Thomas et al. 1986, Batson et al. 1992).

Observations during the *Phobos 2* encounter in 1989 resulted in considerably improved determinations of the density, orbital dynamics, surface color, composition, and texture of Phobos. High resolution images were obtained for regions west of crater Stickney and surface brightness was measured over an extended range of phase angles and wavelengths. From improved estimates of Phobos' mass ($1.08 \pm 0.01 \times 10^{16}$ kg) and volume (5530 ± 300 km^3), its mean density was determined to be 1950 ± 100 kg m^{-3} which is significantly smaller than the value of 2200 ± 200 kg m^{-3} obtained from the *Viking* observations. The density is significantly lower than that of materials with similar spectral reflectances. The smaller density is probably caused by water ice inclusions in the satellite's interior or indicates that the satellite's interior is unconsolidated and porous (Avanesov et al. 1989, Burns 1992). The surface density of 2000 kg m^{-3} as determined from recent radar measurements is close to the bulk

(a) PHOBOS

$$n > \Omega$$
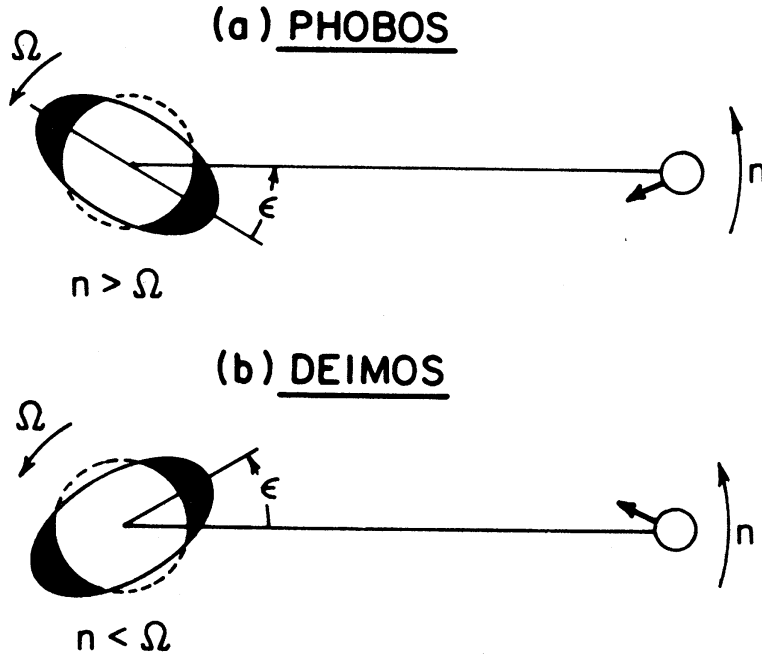
(b) DEIMOS

$$n < \Omega$$

Fig. 9. Tidal bulge retardation of Phobos (a) and Deimos (b). The retardation of the planetwide tidal bulge causes gravitational interactions of Mars with the tide-generating satellites. As to the inner satellite Phobos, its mean motion n surpasses the rotation rate Ω of Mars $(n > \Omega)$, so that the dissipation of tidal strain energy within the Martian interior is balanced by a loss of the satellite's orbital energy causing the orbit of Phobos to shrink over time while its orbital angular momentum is transferred to spin angular momentum of the planet's rotation. In contrast, the mean motion n of the outer satellite Deimos is smaller than the rotation rate Ω of Mars $(n < \Omega)$ slowing down the rotation of Mars and transferring spin angular momentum to the orbital motion of Deimos thereby expanding the orbit of Deimos over time. Therefore, both satellites are evolving away from each other, because dissipation of tidal strain energy causes the orbit of Phobos to shrink by tidal deceleration and, to a much lesser extent, that of Deimos to expand by tidal acceleration (Burns 1992, figure reprinted from Fig. 3, page 1296, from Contradictory Clues as to the Origin of the Martian Moons. In H.H. Kieffer, B.M. Jakosky, C.W. Snyder, and M.S. Matthews, editors, *Mars*, pages 1283–1301, Univ. of Ariz. Press, Tucson; © 1992 by The University of Arizona Press)

density which suggests a uniform distribution of density with depth. The central pressure is calculated to be about 5×10^4 Pa (Thomas et al. 1986).

Tidal interactions between satellites and planets act towards synchronization of the planet's rotation rate and the satellites' rate of revolution if the latter is smaller than the former. The orbital evolution depends on the rate of dissipation of tidal energy in the planet and in the satellite. However, due to the very small sizes of Phobos and Deimos secular changes of their orbital parameters chiefly result from the anelastic properties of the Martian interior. An orbit synchronous with Mars' present rotation rate has a semimajor axis of $a = 6.02 r_p$ where r_p is Mars' surface radius. The almost circular orbit of Deimos ($a = 6.9 r_p, e = 0.0002$) lies near to but beyond the synchronous position and will expand with time and its eccentricity will increase (Fig. 9). Because of the larger distance and the smaller size, however, the secular deceleration of Deimos is less than 1% of Phobos' acceleration, so that the nearly circular orbit remains close to the synchronous position (Burns 1986, Burns 1992)

and has hardly evolved in the past. The orbit of Phobos has a semimajor axis of $a = 2.76r_p$ and an eccentricity of $e = 0.0152$ and lies well inside the synchronous orbit. As seen from Mars, Phobos rises several times per Martian day in the west and moves then rapidly west to east, whereas Deimos moves slowly from east to west across the Martian sky. Dissipation of tidal strain energy within the Martian interior causes a loss of the satellite's orbital energy and an increase of the planet's rotation energy (Fig. 9). Accordingly, the orbit of Phobos will shrink and the eccentricity will increase as well as Mars' rotation rate. The orbit will shrink until the satellite gets destroyed as it passes through the Roche limit.

Combining the differential formulation of Kepler's third law

$$\frac{\dot{a}_i}{a_i} = -\frac{2}{3}\frac{\dot{n}_i}{n_i} \tag{9}$$

where a_i and n_i are the semimajor axis and the mean motions of the satellites, with a simplified model for the tidally-induced changes of the semimajor axis over time

$$\dot{a}_i = 3m_i\frac{k_2}{Q_p}\left(\frac{G}{a_i(M_p + m_i)}\right)^{\frac{1}{2}}\left(\frac{r_p}{a_i}\right)^5 \tag{10}$$

provides an estimate of the product k_2/Q_p of the elastic Love number k_2 and the globally averaged specific dissipation function Q_p^{-1} of the Martian interior from observations of the secular variation $\dot{n}_i$ of each satellite. Primarily using long-term groundbased observations of Phobos' orbital longitude the measured secular rate of acceleration has been estimated to be in the range of 0.00254 to 0.00263 deg a^{-1}. The rate of acceleration accumulated to a longitudinal shift of 15° since its discovery in 1877. According to (9), this corresponds to a steady decrease of orbital distance and suggests that the satellite will be destroyed and the debris hit the Martian surface within the next 40 Ma (Burns 1986, Burns 1992). The mean specific dissipation factor Q_p of Mars was estimated from the secular acceleration rate to be between 50 and 150 for the main tidal period of 5^h32^m (Smith and Born 1976).

A naive backward integration of Phobos' present orbit yields a primordial eccentricity of 0.1 to 0.2 about 4.6 Ga ago. Tidal dissipation in Phobos would even increase this value. Such a large value of eccentricity suggests that the satellite was captured at some time into a large elongate orbit about Mars. The spectral properties of both satellites in terms of their albedos, colors, and spectral reflectivities indeed suggest that Phobos and Deimos are asteroidal rather than terrestrial. These values are similar to those of Jupiter's Trojan asteroids and dark carbonaceous C-type asteroids such as Ceres populating the outer asteroid belt at 2.8 to 3.3 AU distance from the Sun. However, the nearly circular orbit of Deimos argues against capture at least of that satellite. Moreover, Deimos effectively represents a dynamical barrier that limits the evolution of Phobos' elongate orbit. If Phobos once had an apocenter distance beyond Deimos' orbit than it would hardly have survived because the characteristic collision timescale for Deimos and Phobos on interlaced orbits ($\leq 10^3 - 10^6$ a) is much briefer than Phobos' orbit evolution time scale ($\sim 10^9$ a). The most probable solution to this problem is that Phobos' present eccentricity results from relatively recent events. Gravitational resonances with Mars' rotation at 2.9, 3.2, and 3.9 r_p are expected to cause significant jumps in orbital eccentricity and inclination (Yoder 1982, Burns 1992). Therefore, the observed Phobos eccentricity may be due to resonant interaction alone and may be larger than the primordial value. Both orbits would then have never crossed and could

Fig. 10. View of Phobos and crater Stickney at left limb. There is a regular pattern of grooves on the irregularly shaped surface of Phobos. The groove orientation is related to the principal axes of Phobos and symmetric about the prime meridian at 0° longitude pointing to Mars. The grooves on Phobos are less than 30 m deep with the deepest grooves occuring near crater Stickney and 100 to 200 m wide with lengths of nearly 20 km. The morphology of grooves suggests an uppermost loose regolith layer up to 100 m in depths. The groove pattern, however, does not agree with the tidal stress pattern and is difficult to explain by secondary impacts. As a crude approximation, the groove pattern may result from fracturing during the Stickney impact (© *NASA/JPL*)

be of a noncapture origin. This leaves the problem of the satellites' surface properties argueing for capture.

Tidal and rotational accelerations are especially relevant on Phobos and contribute about 40% of its surface gravity. As a consequence, tidally induced environmental processes must be distinguished from processes controlling the distribution of ejecta blocks and downslope migration of regolith in the low-gravity environment of small planetary bodies. The escape velocities of a few m s^{-1} at the surfaces of Phobos and Deimos strongly depend on the specific location and direction. The surfaces of Phobos and Deimos differ from each other in that Phobos is densely cratered and features linear depressions while Deimos is covered by subdued craters filled with up to 20 m of debris fill and subdivided by prominent ridges into three major regions (Thomas et al. 1986, 1992).

The surface of Phobos is dominated by very long ridges (e.g., Kepler Dorsum), some of which are parallel to each other (Fig. 10). The presence of long linear features indicates that the surface gravitity is not sufficiently large to induce relaxation of

the topography on a geological timescale against the satellite's internal strength. The maximum crater densities are comparable to the lunar highlands and close to the saturation limit where the number of new craters balances destroyed older craters of the same size. Brighter materials are deposited at ridge crests and crater rims, whereas darker material is concentrated in low areas. Prominent color variations are essentially absent on both satellites. Deimos reveals large brighter patches and streamers, while on Phobos subdued albedo markings are present. The differences are caused by differences in texture or in composition. The brighter areas are probably composed of finer-grained carbonaceous materials, whereas the darker markings within some craters on Phobos are due to rougher surface textures (Thomas et al. 1986, 1992).

Inhomogeneities of the thermal and spectral properties of Phobos' surface as measured by the *Phobos 2* spacecraft correspond to variable grain sizes of tens to hundreds of micrometers (Ksanfomality et al. 1989). The rapid heating of Phobos' surface following eclipse by Mars indicates very low thermal inertia of the uppermost regolith cover. The low-inertia layer is at least several thermal skin depths in thickness and requires particle sizes of 50 to 100 μm. The depth of the regolith layer on Phobos is variable with layering at depths of about 80 and 150 m. The thinner regolith cover on Deimos is due to the smaller crater density. Regolith downsloping occurs more locally on Phobos, while regolith downsloping on Deimos is relevant on a global scale. Furthermore, the thermal infrared data suggest that about 5% of Phobos' surface is covered by high-inertia, blocky material to a depth of 10 cm. Because of the lower gravity, ejecta blocks are more widely dispersed on Deimos than on Phobos (Clark et al. 1986, Thomas et al. 1992).

3. Physics and chemistry of the Martian interior

Prior to the exploration of Mars by spaceprobes, attempts at modeling the interior structure of the planet suffered from poorly known values of its radius and moment of inertia (e.g., Urey 1952). Improved measurements of the planet's mass M_p, radius r_p, gravitational potential and rotation rate by the *Mariner* and *Viking* spacecrafts provided the geodetical constraints required for models of the interior structure (Born 1974, Bills and Ferrari 1978, Balmino et al. 1982). The most important constraint on the concentration of mass toward the center, the planet's polar principal moment of inertia C, however, is still not known with sufficient accuracy although a recent inversion of *Viking* range data has significantly reduced the uncertainty. Better data that may settle the debate on the value of the moment of inertia factor are expected from the *Mars Pathfinder* mission in 1997. Seismology on the surface of Mars could provide the most reliable constraints on the physical state and the chemical composition of the Martian interior. Not only could the core radius, the crust thickness, and the layering of the mantle be derived from the traveltimes of waves generated by sufficiently strong quakes. If there are marsquakes large enough to excite low harmonic free oscillations of the planet, Okal and Anderson (1978) show that the period of the dominant spheroidal mode $_0S_2$ in case of a solid core would be roughly 2/3 of that in the presence of a completely molten core. Further indicators of a possibly liquid core or core shell as recently suggested by Mocquet et al. (1996) would be the existence and the lateral extent of a seismic shadow zone and the amplitudes of core–reflected phases of nearly vertically incident seismic waves that would be greatly affected. Seismology on Mars would profit from a better signal to noise ratio as compared with terrestrial seismology. Due to the absence of oceans on Mars and

its smaller size a quake with the same signal to noise ratio on Mars can be one to two magnitudes smaller than on Earth. Relatively weak quakes of magnitudes 4 to 5 that have regional significance on Earth would be global events on Mars. A seismology mission to Mars has been studied by Chicarro et al. (1993) and Banerdt et al. (1996). Planetary seismology has recently been reviewed by Lognonné and Mosser (1993).

Interior structure

A number of previous studies have already shown that the mean mantle density would be rather insensitive to the composition and size of the metallic core given a fixed value for the dimensionless moment of inertia factor (Johnston et al. 1974, Göttel 1981, Schubert and Spohn 1990, Schubert et al. 1992). Thus, a reliable determination of the polar moment of inertia factor by a precise measurement of the spin–axis precession period according to (Esposito et al. 1992)

$$\omega_p = \frac{3}{2} \frac{n_{rev}^2}{\Omega} \frac{J_2}{C/M_p r_p^2} \cos\theta \qquad (11)$$

where $\Omega = 2\pi/\tau_{rot}$ is the rotation rate, $n_{rev} = 2\pi/\tau_{rev}$ is the orbital mean motion, θ is the obliquity of Mars, and $J_2 = 1960.454 \times 10^{-6}$ is the observed gravitational oblateness, will provide excellent means to constrain the density of the Martian mantle. Until the precession period of the spin-axis of Mars is accurately determined, estimates of C suffer from assumptions about the magnitudes of the nonhydrostatic contributions, in particular those of the Tharsis Rise, to the oblateness of the Martian gravitational potential. Assuming that Mars is in a hydrostatic state ($J_2^h \approx J_2$), and the hydrostatic value of the gravitational oblateness J_2^h is approximately given by the observed oblateness J_2, $C = 0.376 \times M_p r_p^2$ is calculated from the Radau-Darwin relation

$$\frac{C}{M_p r_p^2} = \frac{2}{3} \left[1 - \frac{2}{5} \left(\frac{4m - 3J_2^h}{m + 3J_2^h} \right)^{\frac{1}{2}} \right] \qquad (12)$$

where m is the equatorial ratio of gravitational to centrifugal acceleration (Cook 1977).

A more realistic estimate of the hydrostatic value of the quadrupole moment $J_2^h = -C_{2,0}^h$, that accounts for the gravitational effect of the crustal updoming of the Tharsis Rise, requires a reduction of the observed J_2 term by non-hydrostatic contributions according to

$$J_2^h = J_2 - 2 \left(\frac{2 - \delta f}{\delta f} \right) J_{2,2} \qquad (13)$$

with the ellipticity term $J_{2,2}$ given by (5). The parameter

$$\delta f = \frac{\delta B - \delta A}{\delta C - \delta A} \qquad (14)$$

measures the triaxiality of a non-hydrostatic ellipsoid ($\delta A + \delta B + \delta C = 1$) superimposed on the principal equatorial moments of inertia A and B and the polar moment of inertia C (Esposito et al. 1992). The assumption of an axisymmetric distribution of topographic loads about Tharsis (Reasenberg 1977, Kaula 1979), based on the spherical harmonic representations of the gravitational potential and the large-scale

topography given in (1) and (4), yields $\delta f = 1$ because of the identity $\delta B = \delta C$. The quadrupole moment is then reduced according to

$$J_2^h = J_2 - 2J_{2,2} \quad , \tag{15}$$

where uncertainties are solely due to deviations from the assumed axial symmetry of Tharsis. In this way, $C = 0.3663 \times M_p r_p^2$ is obtained as the most probable maximum value for the polar moment of inertia (Esposito et al. 1992). If the nonhydrostatic contribution to J_2 is a maximally triaxial ellipsoid (intermediate axis nearly midway between the greatest and smallest axis) as suggested by Bills (1989), then $C = 0.345 \times M_p r_p^2$ which provides a lower bound on realistic values for C. A recent inversion of *Viking* range data by Yoder and Standish (1997) has provided an improved value for the precession rate of the Martian rotation axis. From the precession rate and J_2, $C/M_p r_p^2$ can be estimated and Yoder and Standish (1997) obtained a value of (0.355 ± 0.015) which must be considered as the best estimate at the present time. An improved measurement of the precession rate by two-way X-Band Doppler tracking of the *Mars Pathfinder* lander is expected from the *Mars Pathfinder* mission in mid 1997.

Early compositional and structural models of Mars have used the hydrostatic value of $C = 0.376 \times M_p r_p^2$ and yield comparatively small core mass fractions (Binder 1969, Anderson 1972, Binder and Davis 1973, Johnston et al. 1974). More recent models used $C = 0.365 \times M_p r_p^2$ (Johnston and Toksöz 1977, McGetchin and Smyth 1978, Okal and Anderson 1978, Morgan and Anders 1979, Göttel 1981, Schubert and Spohn 1990, Ohtani and Kamaya 1992) and obtained larger core size estimates and generally less dense but still FeO-rich mantle compositions. In general, these models have core radii around 0.5 r_p, mantle densities of (3440 ± 60) kg m^{-3} corresponding to a FeO-content of 15 wt.% and core mass fractions between 14.8% (pure iron) and 26.3% (pure troilite) (Göttel 1981). Provided the iron content of the Martian mantle exceeds that of the Earth, a minimum value of the mean moment of inertia factor of 0.355 can be expected, if contributions due to a less dense crustal layer overlying the mantle are neglected (Mocquet et al. 1996). The role of sulfur in the core has been recently investigated by Schubert and Spohn (1990) for a two-layered interior structure model of Mars with moment of inertia factors ranging from a value of 0.345 as lower limit to 0.365 as upper limit.

Structural models based on chemical arguments show similar variations in core size estimates. It has been suggested that the addition of about 13 wt.% FeO to terrestrial pyrolite could explain the relatively large mantle density required to satisfy $C/M_p r_p^2 = 0.365$. In particular, this composition of the Martian mantle offers an explanation for ultrabasic mantle-derived partial melts of low viscosity (McGetchin and Smyth 1978). A similar chemical composition of Mars has been calculated by Morgan and Anders (1979) using a chondritic bulk iron content of 26.7 wt.% and some key element abundances representing fractionation processes in the early solar system. This model has a core mass fraction of 19%. The corresponding sequence of mineralogical phase assemblages stable in the Martian mantle has been experimentally established by Kamaya et al. (1993).

From considerations of element correlations in SNC meteorites (Wänke and Dreibus 1988), the Martian interior has been concluded to be composed of two geochemically distinct components, a highly reduced refractory component and an oxidized volatile-rich one. In this model, Mars is differentiated into a FeO-rich silicate mantle containing radiogenic heat sources in terrestrial abundances and a sulfur-rich
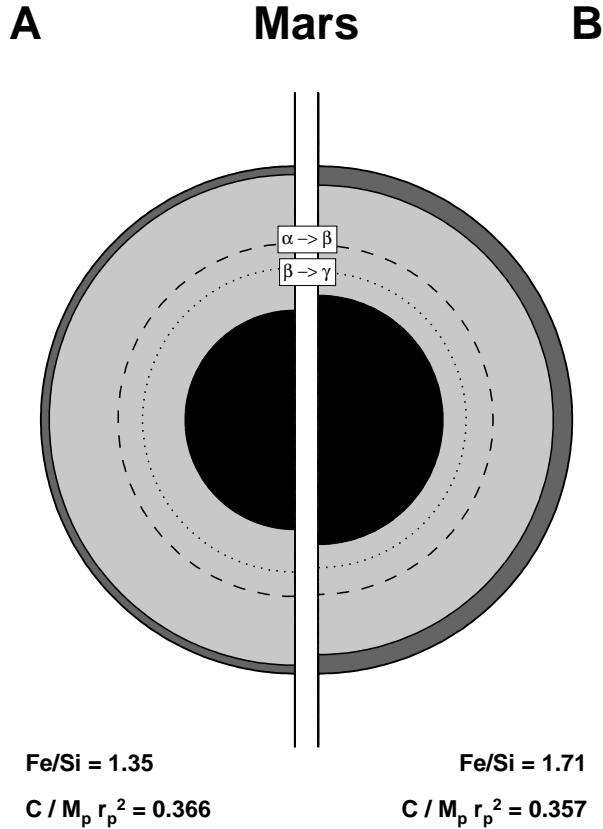
Fig. 11. Comparison of the internal structure of Mars for both models **A** and **B**. The global structures of the two models are similar with a basaltic crust, an upper and a lower mantle separated by the α-olivine to β-spinel transition, and a metallic core. The lower mantle is further subdivided into β-spinel and very thin γ-spinel layers. The models differ significantly in the thicknesses of the crusts and the radii of the liquid cores. Fe/Si and $C/M_p r_p^2$ denote the calculated global iron to silicon ratio and the dimensionless polar moment of inertia factor, respectively

Fe-Ni-FeS core of about 22% of the planet's mass containing about 14 wt.% sulfur and with a core radius of 0.5 r_p. Converting the mantle composition of Dreibus and Wänke (1985) into a pressure-dependent mineralogy, Longhi et al. (1992) divided the Martian mantle like the terrestrial mantle into an upper olivine-rich part, a transition zone composed of silicate-spinel, and a lower perovskite-rich zone. The model provides a mean dimensionless moment of inertia factor of 0.353 and is consistent with the geochemical constraint of a global Fe/Si ratio of 1.71 representative of the composition of carbonaceous chondrites. Recently, Bertka and Fei (1997) conducted high-pressure and high-temperature experiments using synthetic mineral mixtures according to the mantle composition of Dreibus and Wänke (1985) to obtain the sequence of mineralogical phase assemblages stable in the Martian mantle at elevated temperatures and up to core-mantle boundary pressures. The upper part of the mantle then contains olivine, clinopyroxene, and garnet, whereas orthopyroxene is only present at pressures

below 9 GPa. In the mantle transition zone at pressures above 13.5 GPa, β-spinel and clinopyroxene are subsequently replaced by γ-spinel and majorite until completion at about 17 GPa. Furthermore, a perovskite layer of a few hundred km thickness is possible at the base of the mantle. Its existence and its stable phase assemblage not only depends on the core-mantle boundary pressure, i.e., the size and composition of the core, but also on the temperature in the deep mantle. A sufficiently hot lower mantle with temperatures above 2100 K would have a layer of Mg-Fe silicate perovskite, $CaSiO_3$ perovskite, magnesiowüstite, majorite, and stishovite (Bertka and Fei 1996).

In Fig. 11, two models of the present interior structure of Mars are compared using identical sets of material parameter values for crust, mantle, and core as derived from geochemical analyses of SNC meteorites. As a more complete discussion is given elsewhere (Sohl and Spohn 1997), only a few selected results are presented here. The first model is optimized to satisfy the most probable maximum polar moment of inertia factor of 0.3663 (model A), while the second model satisfies the geochemical requirement of a chondritic bulk composition in terms of the bulk ratio Fe/Si=1.71 (model B). This model has a polar moment of inertia factor of 0.357. The differential equations for the mechanical and thermal structure are based on the fundamental conservation laws for mass, moment, and energy and are solved numerically together with an isothermal Murnaghan-Birch type equation of state. The global structures of the two models are similar with a basaltic crust, an upper and a lower mantle separated by the olivine to spinel transition, and a core. The lower mantle is further subdivided into β-spinel and γ-spinel layers with less substantial differences in the locations of the olivine–β-spinel transition and the β-spinel to γ-spinel phase boundary. Almost half of the bulk iron by mass is provided by the core, which is found to be entirely liquid lacking a solid inner core and comprises about 15% of the planet's mass for model A and 21% for model B.

In Fig. 12, relative core sizes and dimensionless moment of inertia factors for both models A and B are compared with results of previous work. Wänke and Dreibus (1988) as well as Schubert and Spohn (1990) calculated two–layered structural models consisting of metallic cores overlain by silicate mantles and ignored the influence of compression, thermal expansion, and the existence of high–pressure phase transitions in the mantle. As becomes obvious from an inspection of panel (a) these models overestimate core size. Models that use an equation-of-state such as those of Ohtani and Kamaya (1992), Longhi et al. (1992) and Sohl and Spohn (1997) typically obtain smaller cores. Panel (b) illustrates the fact that a better knowledge of the hydrostatic value of Mars' polar moment of inertia factor is needed because on grounds of theoretical predictions alone there is too broad a range of possible estimates imposing no firm constraint on the interior structure of the planet.

Although the crust thicknesses of 110 km found for model A and 250 km found for model B may be considered large, there are several arguments in favour of a thick Martian crust. In the absence of reliable seismic measurements of crust thickness, gravity and topography data are used to estimate the mean thickness of the Martian crust. Contributions to gravity anomalies arise from lateral variations in density and surface topography and from undulations of the crust-mantle boundary (Bills and Ferrari 1978, Kiefer et al. 1996). Provided that the relatively low gravity anomalies observed in large areas of the northern lowlands and southern highlands (with the exception of Tharsis) can be interpreted in terms of Airy–type isostatic compensation of the global crustal dichotomy, a global mean crustal thickness of about 100 km has been inferred (Janle 1983). This corresponds to a crust volume normalized to planetary volume of more than 10 times that of the Earth (Esposito et al. 1992).
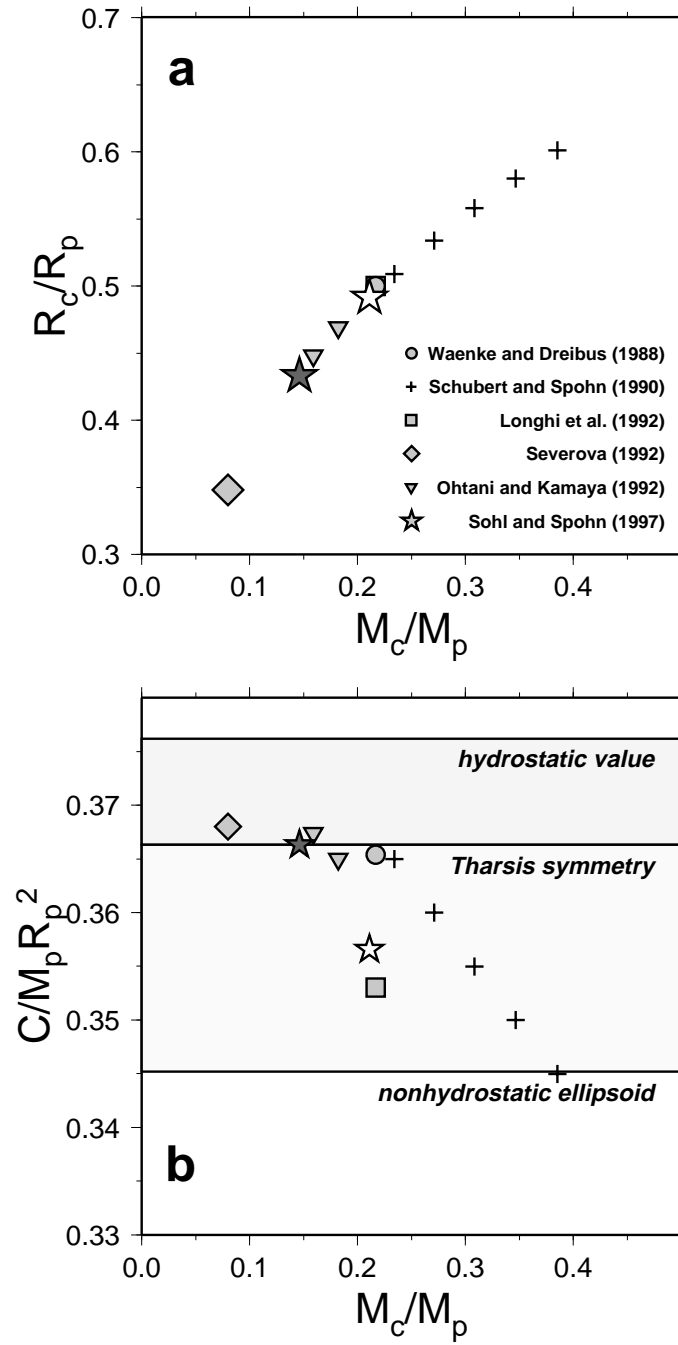
Fig. 12. Comparison of relative core sizes and dimensionless moment of inertia factors for several models of Mars' interior structure constrained by the SNC chemistry. Note that the filled asterisk designates model **A** while the open asterisk indicates model **B**

The mineralogy of the SNCs and ALH84001 may provide additional clues to the thickness of the crust. While ALH84001 does not allow an absolute crust thickness estimate for the ancient southern hemisphere since it is a cumulate rock, its composition of 96% orthopyroxene suggests a high degree of partial melting and thus a large crust volume.
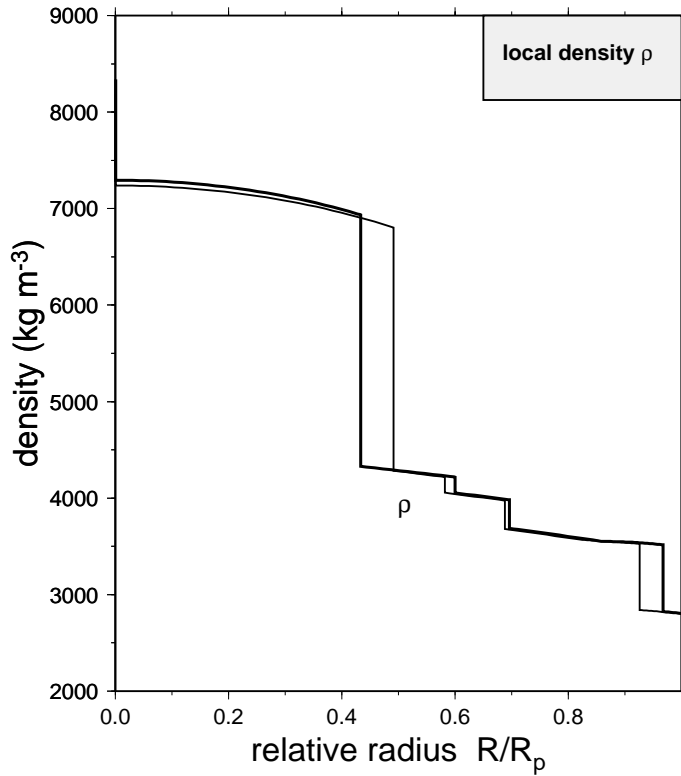

Fig. 13. Radial distribution of density for model **A** (heavy curve) and model **B** (light curve). Note that there is little difference between crust and mantle densities in the two models despite of significant differences in crust thicknesses and core radii

Despite significant differences in crust thicknesses and the core radii, the variation of density with depth is similar for both models. The density ρ as a function of the radial distance from the planet's center is shown in Fig. 13. Because ρ depends more strongly on pressure than on temperature, a feature common to planetary bodies, the density distribution is calculated by using an isothermal fourth-order Eulerian finite strain Murnaghan-Birch equation of state and by applying temperature corrections through a calculation of the thermal pressure contribution (Stacey et al. 1981). The density increases almost linearly with depth in the mantle and crust layers. Because the material properties significantly vary between core, mantle, and crust materials, the density profiles reveal prominent discontinuities by 600 kg m^{-3} at the crust-mantle boundary and by 3000 kg m^{-3} at the core-mantle boundary. In contrast, mantle density discontinuities caused by pressure-induced phase transformations cause much smaller density discontinuities.
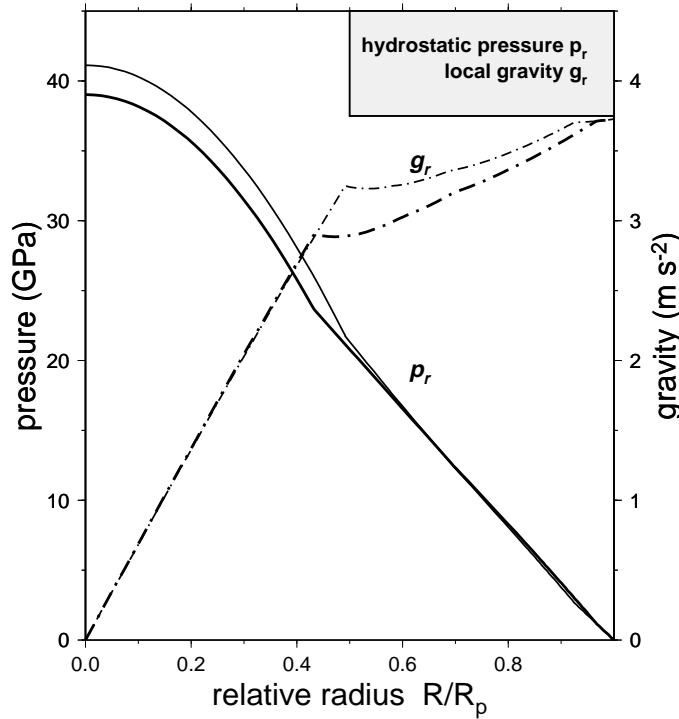
Fig. 14. Radial distribution of hydrostatic pressure and gravitational acceleration for model **A** (heavy curve) and model **B** (light curve). There are small but significant differences in the pressure in the core between the two models, mainly caused by differences in the core masses

The olivine to β-spinel transformation occurs at a relative radius equal to 0.7 corresponding to a depth of about 1000 km, while the β-spinel to γ-spinel transition is situated close to relative radius 0.6, several hundred kilometers above the core-mantle boundary. These transitions occur at a greater depth than in the Earth's mantle simply because of the lower pressures in the Martian mantle. The smaller pressure gradient will have the additional consequence that the transitions will be spread over a wider depth range. Hence the mantle phase transition region of Mars is probably marked by two exothermic phase transformations above the core-mantle boundary, thereby providing a highly efficient acceleration mechanism for vertical mantle flow sufficient for locally elevated viscous dissipation and partial melt generation (see below and Zhou et al. 1995, Breuer et al. 1996).

The radial variations of hydrostatic pressure and gravitational acceleration are shown in Fig. 14. The pressure increases linearly with depth throughout the crust and mantle and parabolically in the core resulting in central pressures of about 40 GPa. The pressure required for the phase transformations to take place is 13 GPa at the $\alpha-$olivine–β-spinel transition and 18 GPa at the β-spinel–γ-spinel transition. However, pressure and temperature in the mantle seem to be not sufficient for the spinel–perovskite transition to occur in the 22 to 24 GPa range (Leliwa-Kopystyński and Bakun-Czubarow 1980, Chopelas et al. 1994). If the core were solid, however, experimentally determined structural changes of solid iron sul-
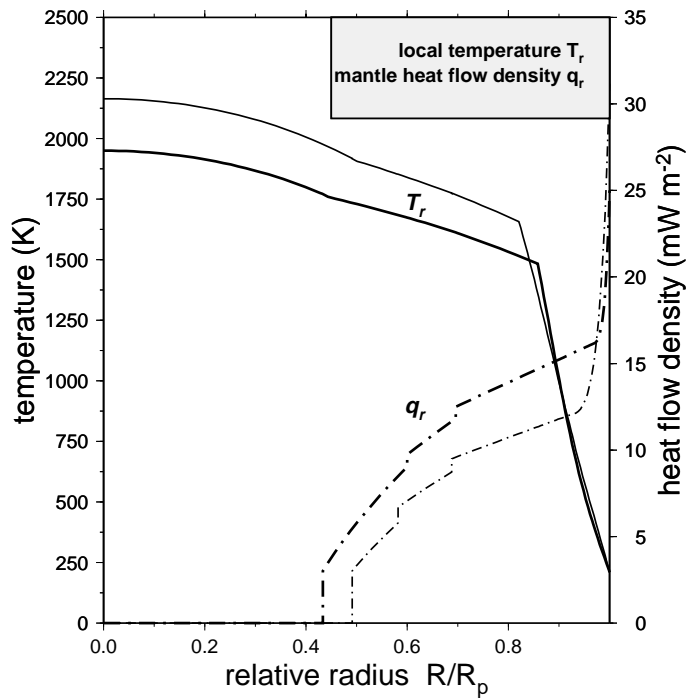
Fig. 15. Radial distribution of temperature and heatflow density for model **A** (heavy curve) and model **B** (light curve). The heat flow from the core into the mantle is taken to be 3 mW m^{-2} in accordance with results of thermal history calculations by Spohn (1991) and by Breuer et al. (1993). In the crust, the heat flow density increases rapidly to surface values between 25 and 30 mW m^{-2} as a consequence of the crust's strong enrichment in radiogenic heat sources relative to the underlying mantle

fide at Martian core pressures and temperatures would imply a significant reduction in core size. Fei et al. (1995) suggest that a lower mantle perovskite layer of significant thickness could be present under these circumstances. The gravitational acceleration increases linearly with radius throughout the core and approximately parabolically through the mantle.

In Fig. 15, the present-day areotherms for both models are shown together with the radial distribution of mantle heat flow density. The temperature increase across the crust and thermal lithosphere, which represents the thermally conductive outermost layer of the planet, is found to be about 1300 to 1400 K. The thermal lithosphere is subdivided into the uppermost rheological lithosphere, which is characterized by an elastic flexural response to the emplacement of surface loads, and the upper cold thermal boundary layer of the convecting mantle, where viscoelastic relaxation in the presence of subsolidus creep becomes effective on a geologic time scale (e.g., Spohn 1991).

The thickness of the rheological lithosphere is about 300 km roughly in accordance with thermal evolution calculations, which suggest the present rheological lithosphere of Mars to be some 100 km thick, depending on the true amount of volcanic heat advection during the early stages of evolution (Schubert and Spohn 1990, Spohn 1991, Schubert et al. 1992). Using a two–stage evolution model of the for-

mation of the global crustal dichotomy of Mars through mantle differentiation, Breuer et al. (1993) have found lithosphere thicknesses in the 150- to 250-km range beneath the northern lowlands, depending on the amount of thermal blanketing attributed to the ancient southern highland crust. A variety of studies (e.g., Solomon and Head 1982, Comer et al. 1985) using elastic flexure theory challenged the earlier conclusion that local features such as large single volcanic loads accompanied by circumferential narrow grabens would require rheological lithosphere thicknesses between 20 and 60 km. Topographic features on a regional scale such as Olympus Mons, Elysium Planitia, and Isidis basin, however, appear to imply lithospheres being 100 up to 400 km in thickness (Thurber and Toksöz 1978, Banerdt et al. 1982, Willemann and Turcotte 1982, Janle and Jannsen 1986). On a global scale, the rheological lithosphere thickness has been concluded to be greater than 150 km (see Janle and Meissner (1986) for a review). However, it should be kept in mind that these thickness estimates are restricted to the time of load emplacement and graben formation, thereby imposing some additional constraints on the thermal history a specific surface feature may have undergone (Banerdt et al. 1992).

The cold thermal boundary layer of mantle convection underneath the lithosphere is found to be 150 to 200 km thick, resulting in a mean thermal lithosphere thickness of about 500 km. The subsequent adiabatic temperature rise across the convecting upper mantle up to the olivine–β-spinel transition is about 150 K. In the lower mantle the adiabatic temperature increase is about 100 K. The temperature at the core-mantle boundary is found to be in the range between 1750 and 1900 K. The adiabatic temperature distribution throughout the core results in central temperatures close to 1950 K (model A) and 2150 K (model B), respectively.

Because model B requires a crust layer more than twice as thick as that for model A, the mantle in model B is about 3 times more depleted in radioactive elements than the model A mantle. As a consequence, the heat flow density increases much more rapidly with radius in model A. The heat flow from the core into the mantle is taken to be 3 mW m^{-2} in accordance with results of thermal history calculations by Spohn (1991) and by Breuer et al. (1993). There are small jumps in heat flow density at relative radii 0.6 and 0.7 due to the release of latent heat at the olivine–spinel transitions. In the crust, the heat flow density increases rapidly as a consequence of the crust being enriched in radiogenic heat sources with respect to the mantle. The corresponding surface heat flow density of 25 to 30 mW m^{-2} compares well with thermal evolution models, some accounting for mantle differentiation and crust formation, which give present-day heat flow values in the range between 10 and 40 mW m^{-2} (Stevenson et al. 1983, Spohn 1991, Breuer et al. 1993).

Figure 16 shows the seismic velocity structure in terms of the compressional P- and transversal S-wave velocities

$$v_p = \sqrt{\frac{K_S + \frac{4}{3}G}{\rho}} \tag{16}$$

and

$$v_s = \sqrt{\frac{G}{\rho}} \quad , \tag{17}$$

where K_S and G designate adiabatic bulk modulus and shear modulus, respectively. The velocities increase linearly in the crust and mantle layers and parabolically in the core. The rate of increase with depth of the P and S wave velocities is considerably
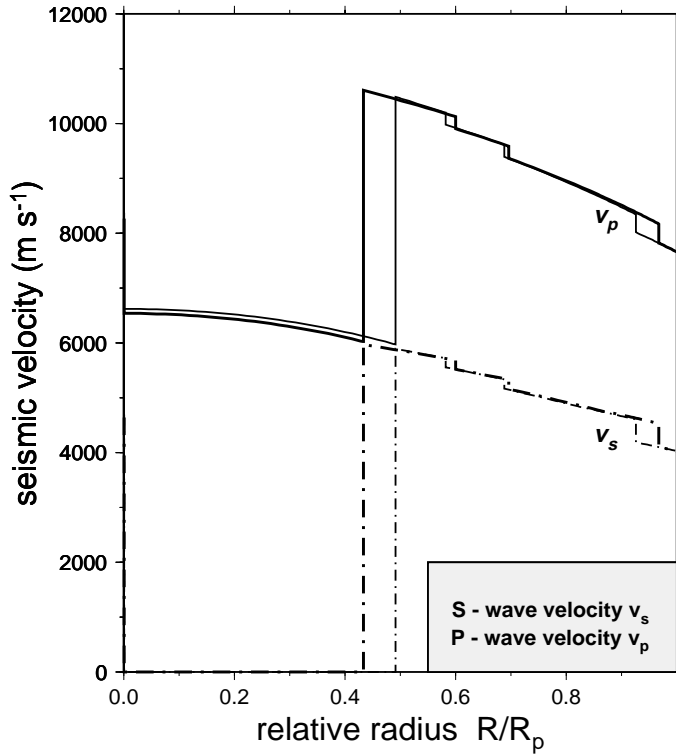
Fig. 16. Radial distribution of seismic velocities for model **A** (heavy curve) and model **B** (light curve). Since in both models the core is found to be entirely liquid, the propagation of transversal seismic waves is prevented

smaller than in the Earth because of the lower rate of increase of pressure with depth caused by the smaller mass of the planet. The P wave velocity in the crust is about 7.7 km s^{-1} and the S wave velocity is 4 km s^{-1}. In the upper mantle, v_p increases from 8.3 to 9.4 km s^{-1}, while v_s increases from 4.6 to 5.2 km s^{-1}. There are significant velocity increases at the olivine–spinel phase transitions to values of 10 and 5.5 km s^{-1} for v_p and v_s, respectively. The P wave velocity in the core is significantly smaller and increases from 6.0 km s^{-1} at the core-mantle boundary to 6.5 km s^{-1} at the center. Since in both models the core is found to be entirely liquid, the propagation of transversal seismic waves is prevented.

Dynamics and Evolution

The thermal evolution of a terrestrial planet depends on the internal heat sources and, to a large extent, on the dynamics of its mantle through which heat is transferred by subsolidus convection. An understanding of the thermal evolution is vital since most interior processes including the dynamics of the mantle depend on temperature and some on energy flow rates. For instance, the history of the planet's endogenic activity, manifested in its tectonic structures of volcanic origin, as well as the history

of the magnetic field depend on the thermal evolution since the underlying processes of melt generation and dynamo action depend on temperature and on the rate of heat transfer through the mantle. The main internal heat sources include accretional heat, potential energy released upon core formation, radiogenic heat produced during the decay of radioactive isotopes, and potential energy and latent heat released as the core possibly differentiates and solidifies.

The accretional heat is the energy accumulated during the burial of heat by impacts as the planet grows through the accretion of planetesimals. During accretion a temperature profile is generated for which temperature increases from the center towards the surface. This profile is quite different from the temperature profiles derived for evolved, present day terrestrial planets (e.g., Figs. 15 and 22). The accretion temperature profile follows naturally from the dissipation rate of kinetic energy upon the impact of planetesimals growing with the mass of the planet. Some early thermal evolution models (see Basaltic Volcanism Study Project (1981) for a review) assumed that core formation took a few Ga to complete and that the evolution started with the accretion temperature profile. In these models, the interior heats up as a consequence of heat generated by radiogenic elements and as a consequence of the deep interior being a heat trap. As temperature increases above the iron melting point, core formation begins. Dissipation of potential energy of the iron moving towards the center increases the temperature and provides a positive feedback. The process is furthered by the temperature dependence of the mantle rheology.

It is commonly accepted that core formation is a comparatively rapid process since the positive feedback between dissipation, flow of iron, and temperature dependent viscosity should lead to runaway core formation (Stevenson 1981). This conjecture is supported for Mars by the isotope systematics of the SNC meteorites which require early core formation about 4.6 Ga ago (Chen and Wasserburg 1986), either contemporaneous with accretion or within a few 100 Ma thereafter. It is further supported by the evidence of early outgassing and an early atmosphere (Owen 1992). Most recent models of Mars' thermal evolution therefore assume that the planet accreted rapidly and differentiated early, within the first 100 Ma, into a core, a mantle, and a crust. In that case the initial temperature profile is inverted rapidly to decrease from the center towards the surface. Since core formation can be quite energetic, it would heat the entire interior by 300 K (Solomon 1979), the young planet is assumed to be relatively hot and to cool during the following evolution. Schubert et al. (1992) have discussed the tectonic evidence for global contraction which implies global secular cooling.

After accretion and core differentiation most of the internal heat is generated by the decay of the radiogenic isotopes of U, Th, and K. It is commonly assumed that these elements occur in the mantle and the crust (e.g., Schubert et al. 1992). However, it is possible that the core contains some radioactive elements that it accreted during core formation as the iron moved towards the center. The radioactive elements are lithophile, i.e. they tend to be enriched in melts. The isotope characteristics of the SNC meteorites indicate that there are at least three reservoirs with differing concentrations of radioactive elements (Jagoutz 1991). Because they are lithophile, the crust is enriched in these elements through magmatic activity by which the crust grows. The mantle can be identified with the most depleted reservoir (Jagoutz 1991). The most enriched reservoir could be the crust. The enrichment factor of radioactive elements in the basaltic crust with respect to the primitive concentration is about 5. The third reservoir with a medium concentration could be the lower lithosphere as Jagoutz (1991) suggested. Breuer et al. (1993) proposed that the enriched reservoir could be the ancient southern hemisphere crust, the formation of which could have severely

depleted the mantle. The northern hemisphere crust in their scenario is identified with the reservoir of intermediate depletion. In any case, it is reasonable to assume that the mantle is significantly depleted. Breuer et al. (1993) assume that the main contribution from the mantle to the present surface heat flow is secular cooling and that only a smaller part is due to radioactivity. The mantle looses its heat to the crust through which it is conducted to the surface and eventually radiated into space. In addition, the mantle is heated by heat flow from the core. Freeze-out of an inner core may provide a non-negligible heat source although it is widely accepted that the lack of a growing inner core provides the best explanation for the absence of a present significant magnetic field (see below and Schubert and Spohn (1990)).
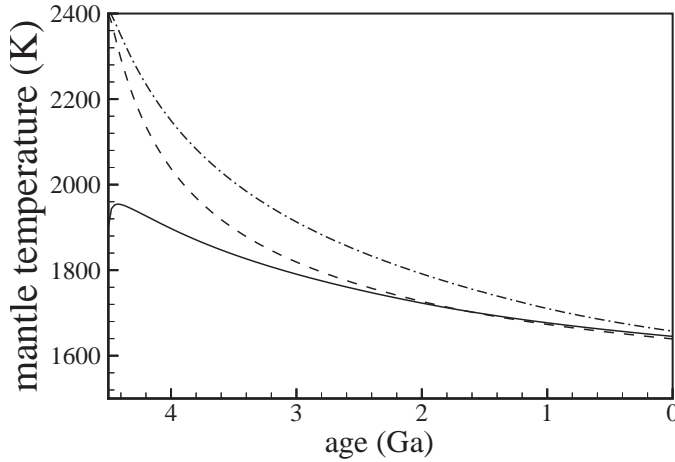

Fig. 17. Martian mantle temperature as function of time according to Breuer et al. (1993). Models have been calculated with an initial temperature of 1900 K (solid line) and 2400 K (dashed and dash-dotted lines). A model with an early depletion of 80% of the radioactive elements in the mantle (dash-dotted line) and two models without an early depletion (solid and dashed lines) are shown.

Recent thermal evolution models have used parameterized mantle convection schemes based on a simple Nusselt-Rayleigh number relationship. The Nusselt number Nu is a dimensionless measure of the surface heat flow. It is defined as

$$Nu = \frac{<q>d}{k\Delta T} \tag{18}$$

where $<q>$ is the average surface heat flow, d is the mantle thickness, k its thermal conductivity, and ΔT the temperature difference across the mantle. Nu measures the heat flow carried by convection relative to that transferred by conduction. The Rayleigh number Ra indicates the vigour of convection. For a fluid heated from below it is defined as

$$Ra = \frac{\alpha g \Delta T d^3}{\kappa \nu} \tag{19}$$

where α is the thermal expansion coefficient, g is surface gravity, κ is the mantle thermal diffusivity and ν is the mantle kinematic viscosity. These thermal evolution models focus on differing aspects of the evolution: Stevenson et al. (1983) and Schubert and Spohn (1990) focus on the core, magnetic field generation and the possible

effects of inner core growth. Crust differentiation and the removal of radioactive elements from the mantle was studied by Spohn (1991) and Schubert et al. (1992), while Breuer et al. (1993) attempted to incorporate the dichotomy together with an early crust differentiation event. The cooling histories calculated from these models show the common feature of monotonous exponential decreases in heat flow and temperature accompanied by a compatible increase in mantle viscosity. Following an early period of rapid cooling is a phase of gradual, slow cooling (Fig. 17). Present potential mantle temperatures in these models are in the range of about 1600 to 1800 K. The potential mantle temperature is the mantle temperature extrapolated along an adiabat to surface pressure. The present surface heat flow is around 20 to 35 mW m^{-2}. Estimates of the present rheological lithosphere thickness vary between 100 to 400 km; the higher values being the results of significant magmatic heat transfer and/or of strong upward differentiation of radioactive elements from the mantle into the crust. As a consequence of the crustal dichotomy, variations in the lithosphere and the crust thickness, and the surface heat flow between the northern and southern hemisphere can be expected (Breuer et al. 1993). These authors find that they can reproduce the albeit uncertain rates of magmatic activity in the northern hemisphere.

The model of Schubert and Spohn (1990) offers an explanation for the apparent lack of a self-sustained magnetic field on Mars. The model extends that of Stevenson et al. (1983) by exploring a larger area of parameter space. In these models the existence of a dynamo is derived by considering the power available for the dynamo to overcome Ohmic dissipation. The thermal power P_d derived from a convecting, crystallizing core is given by

$$P_d = E_{grav} \frac{dm}{dt} + \gamma_{therm} \left(L \frac{dm}{dt} + \frac{dE_{therm}}{dt} - F_{cond} + Q_c \right) \tag{20}$$

where E_{grav} is the gravitational energy released upon inner core growth, dm/dt is the rate of inner core growth by mass, γ_{therm} is an average Carnot efficiency factor approximately equal to 0.05 (Stevenson et al. 1983), L is the latent heat of core solidification, dE_{therm}/dt is the time rate of change of core heat content, and F_{cond} is conductive heat flow down the core adiabat which is not available to drive the core dynamo and Q_c is the possible radiogenic heat source density in the core. In writing (20) it is assumed that the fluid outer core contains an alloy of Fe and S. The inner core would consist almost of pure iron. The compositional difference gives rise to the first term in (20). Moreover, the compositional difference induces convection driven by gradients in sulfur concentration since as long as the inner core grows sulfur is released at the boundary between the inner and outer cores. Compositional convection may drive the dynamo very effectively since it would not be subject to the Carnot efficiency factor.

If Mars lacks an inner core then the existence of a dynamo requires that

$$\frac{dE_{therm}}{dt} - F_{cond} + Q_c > 0 \tag{21}$$

When ($dE_{therm}/dt - F_{cond} + Q_c$) becomes zero, the core will cease to convect and the dynamo will be shut down. The heat flow from the core is determined by the ability of the mantle to remove heat from the core, that is by the vigor of mantle convection. Schubert and Spohn (1990) using the iron melting data of Usselman (1975) and a parameterized convection scheme to model Martian mantle convection find that the core remains liquid if the sulfur content is at least 15 wt.% for reasonable

values of mantle viscosity. They further find the core to cease convecting under these circumstances after about 3 Ga of evolution. These authors neglected the possible contribution to the energy balance from radiogenic heat sources in the core. Inclusion of heat sources would reduce the threshold value for the sulfur content for a liquid core by a few wt.%.

The former evolution models tacitly assume that the planform of convection is quasi-steady and lacks any strong time dependence. Moreover, the models neglect the olivine-spinel and the spinel-perovskite phase transitions the presence and depths of which we have discussed earlier in the paper. Recent calculations using finite amplitude convection codes that give both the planform of convection as well as the temperature distribution in the mantle show significant effects of the phase transitions on the convection flow field. These models suggest a significant time dependence of the flow and the temperature distributions. The time dependences will affect the thermal evolution if the variations occur on the relevant time scales as they do in the calculations. It is important to note that the olivine-spinel transitions are exothermic while the spinel-perovskite transition is endothermic. In general, an exothermic phase transition will accelerate flow crossing the boundary while an endothermic phase transition will retard the flow. These effects may partly or completely be compensated by latent heat releases and consumptions. What actually happens to the flow at the phase transformation depends on local values of buoyancy, temperature and flow velocity. The models presented below will illustrate these effects. An important feature of the models is that, albeit for differing reasons, both types of phase transitions, exothermic and endothermic, tend to decrease the number of upwelling plumes (Weinstein 1995, Harder and Christensen 1996, Harder 1997, Breuer et al. 1996, Breuer et al. 1997b). This is in accordance with the pattern of volcanism on Mars, which is dominated by the two centers Tharsis and Elysium. This pattern of surface volcanic features and the apparent stability of the volcanic activity over the past aeons suggests a small number of steady plumes (Matyska et al. 1996). Mars differs in that respect from both the Earth and Venus where the pattern of surface volcanism is much more widespread and changes with time. The time dependence of Martian mantle convection has probably been reflected in a time dependence of volcanic mass flow. In the following, we present representative results of 2D and 3D convection calculations. These calculations are still too demanding in terms of computer power to allow the calculation of complete evolution models. Rather, we will use the results to discuss possible thermal evolution scenarios. The models are characterized by two parameters: the mean Rayleigh number and the dimensionless surface temperature T_o. The mean Rayleigh number is calculated by averaging depth dependent parameters that enter the definition given in (19). T_o is the dimensionless temperature scaled by ΔT of the base of the stagnant lithosphere below which the mantle flows over geologic time. The value of the basal lithosphere temperature is around 1200 K.

Figure 18 to 22 show results of these calculations in terms of temperature fields, stream functions, vertical mass fluxes at the phase boundaries, and temperature profiles. An 2D axisymmetric spherical-shell model based on the extended Boussinesq approximation (Machetel and Yuen 1988) and a 3D compressible spherical-shell model (Zhang and Yuen 1996) have been used, where the effects of viscous dissipation and adiabatic heating and cooling are included. To model the effects of the phase transitions on the flow, an effective thermal expansivity $\overline{\alpha}$ and an effective heat capacity $\overline{C_p}$ were used to simulate the changes in buoyancy across the phase transition (Christensen and Yuen 1985). Latent heat release and consumption in material that crosses the phase transitions are included in this formulation. The internal structure
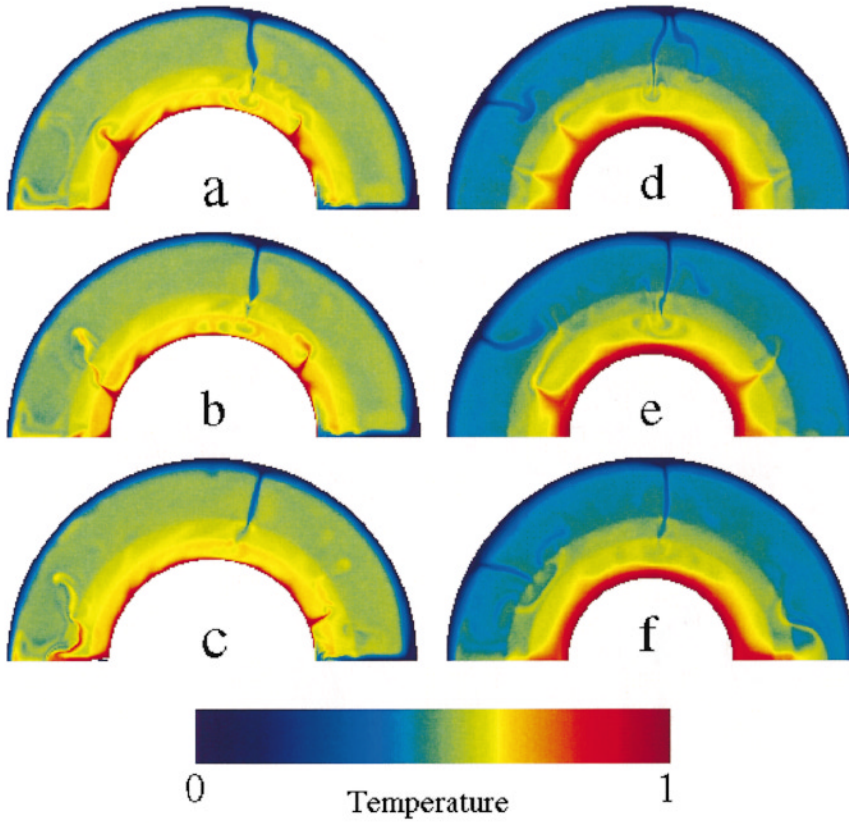
Fig. 18. (a–c) Temperature fields for a model with two exothermic phase transitions at radial distances of $r_{\alpha/\beta} = 0.7 \times r_p$ and $r_{\beta/\gamma} = 0.6 \times r_p$ from the planet's center. (d–f) Temperature fields for a model that includes the spinel–perovskite transition at $r_{sp/per} = 0.45 \times r_p$ in addition to the two exothermic phase transitions. Both models have been calculated assuming a mean Rayleigh number $<Ra>$ of 5×10^6 and dimensionless surface temperature $T_o = 1.2$. The snapshots are shown for t= (a) 0.851×10^{-2}, (b) 0.860×10^{-2}, (c) 0.865×10^{-2} (d) 0.839×10^{-2}, (e) 0.855×10^{-2}, and (f) 0.876×10^{-2}. The dimensionless time of 0.001 corresponds to 360 Ma

assumed for these calculations corresponds to the models discussed earlier in this paper with a core radius of $r_c = 0.5 \times r_p$ and the two exothermic phase transitions (α-to-β-spinel and β-to-γ-spinel) are taken to be located at radial distances of $r_{\alpha/\beta} = 0.7 \times r_p$ and $r_{\beta/\gamma} = 0.6 \times r_p$, respectively.

Upwelling plumes that cross the exothermic phase transitions lose part of their buoyancy due to the consumption of latent heat. These weakened plumes show the tendency to merge and generate a few stronger and larger plumes. Snapshots of the temperature field taken at subsequent time steps for the 2D model (Fig. 18a,b) demonstrate this effect. In the axisymmetric model the strong plumes are preferentially located at the poles. This restriction does not apply in a fully three-dimensional spherical geometry. Breuer et al. (1997a) have tested the behavior of the mantle flow
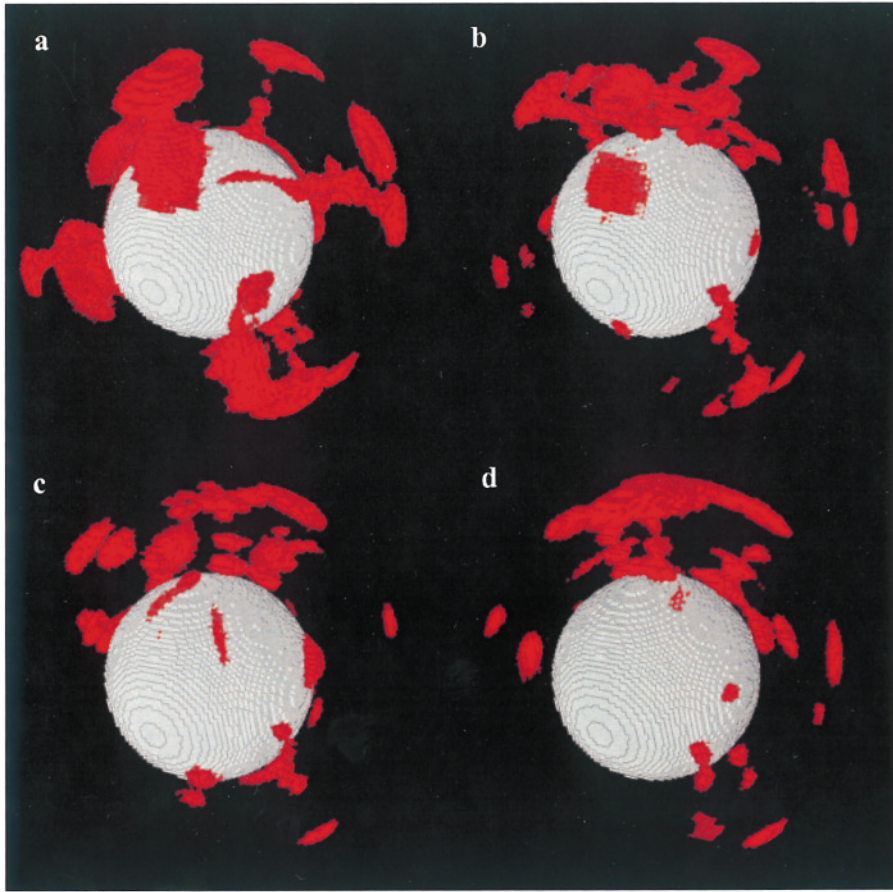
Fig. 19. Positive values of the temperature difference ($\delta T = T - <T(r)>$) which indicate hot upwelling mantle material are shown for a 3D-convection calculation that includes the effects of the two exothermic phase transitions. $<Ra> = 8 \times 10^5$ and $T_o = 1$. The radial distances of the phase transitions are as in Fig. 18 a–c. The snapshots are shown for t= (a) 1.59×10^{-2}, (b) 2.15×10^{-2}, (c) 2.34×10^{-2} (d) 2.76×10^{-2}. The dimensionless time of 0.01 corresponds to 900 Ma

in a 3D calculation. Here, a similar effect of plume merging can be observed: In addition to occasionally appearing upwellings which disappear after a few million years (Fig. 19), one stable area of plumes can be identified which is stabilized by attracting some of the smaller upwellings.

The reduction of the number of strong plumes is associated with a partial layering of the flow induced by the exothermic phase transitions. This layering is caused by a bistable pattern of alternating blocking and acceleration of the flow across the phase boundaries. Convection cells separated by the phase transitions are observed that degenerate on occasion to cells comprising the whole mantle (Fig. 20a,b). The vertical mass flow across the two exothermic phase transitions (Fig. 21a) oscillates between flow blocking and acceleration and shows a strong time dependence. The quasi–periodic alternations between flow blockage and acceleration may have ramifications
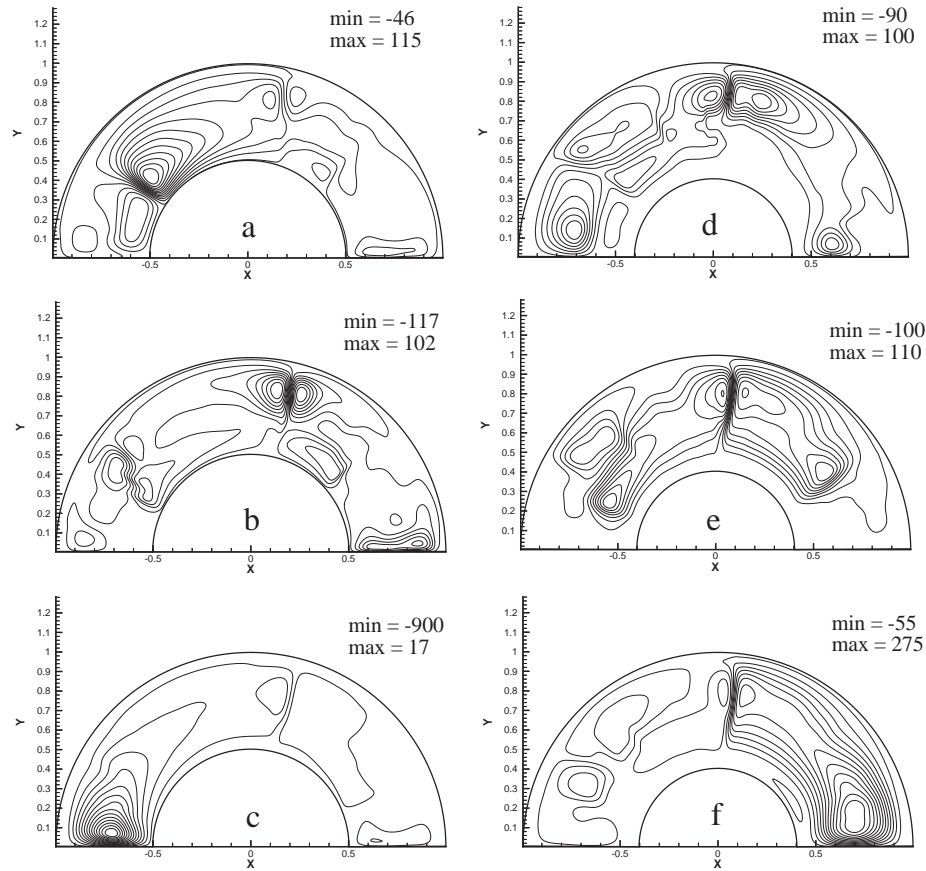
Fig. 20. Stream functions of the mantle flow corresponding to Fig. 18 The numerical values indicate the minimum and maximum values of the stream function. The range of values is distributed equally between 15 contour lines in each panel

on the time dependence of the Martian volcanic activity and suggest that active periods separated by periods of quiescence are likely.

As we discussed earlier, the existence of the endothermic phase transition strongly depends on the mantle temperature and the core size. Although the case for a perovskite layer in the present Martian mantle appears to be marginal at best, there is the definite possibility that such a layer existed in the early Martian mantle when temperatures were higher, possibly 2100 K or more. It is also possible that the core grew after the early differentiation by a few tens to hundred km in size over the history of the planet although that conjecture may be in conflict with the lead isotope data. Results by Breuer et al. (1996) suggested that part of the lower mantle was molten in the early history. To illustrate the effect of the endothermic spinel-perovskite transition near the core–mantle boundary on the flow, Breuer et al. (1997b) have examined a model with a smaller core of $r_c = 0.4 \times r_p$ and varying depths of the spinel-perovskite transition. We show the results of a representative model with the spinel to perovskite transition
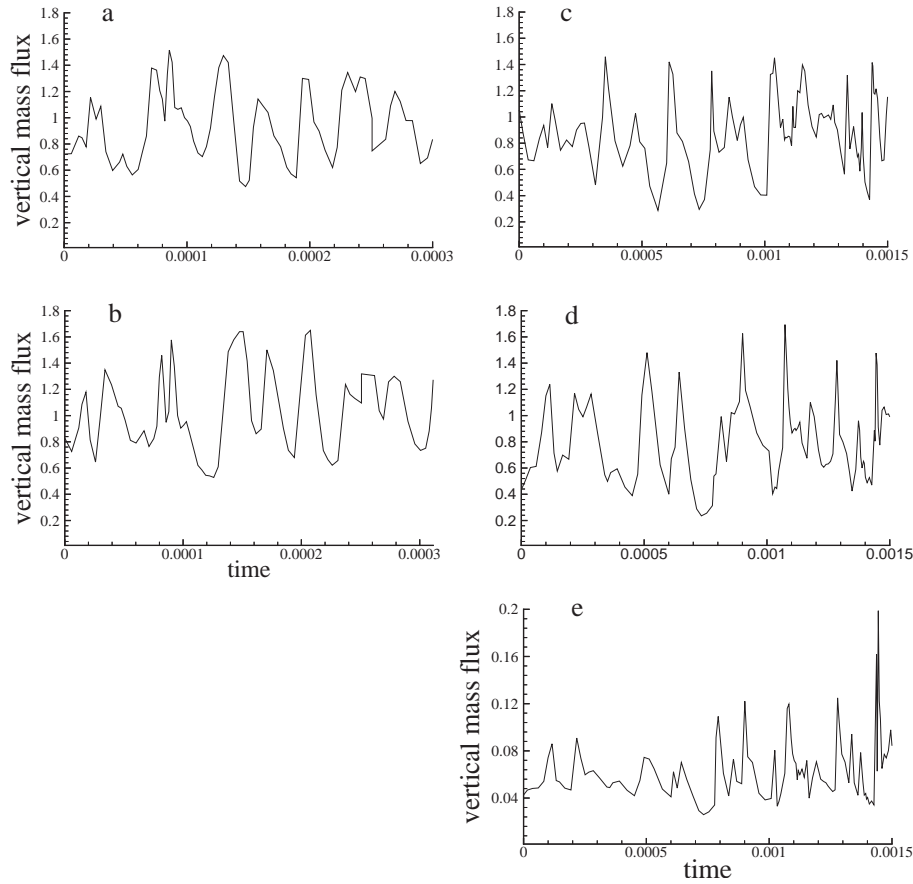
Fig. 21. Time-series of vertical mass flux at the relevant phase boundaries. The vertical mass flux is defined as the ratio between the square of the vertical velocity at the phase boundary and the square of the mean convection flow speed. Results are shown for two models corresponding to the models shown in Fig. 18 and 20: (a,b) The model with the $\alpha - \beta$ and $\beta - \gamma$ transition. Plate a) shows the mass flux at the $\alpha - \beta$ transition while plate b) shows the mass flux at the $\beta - \gamma$ transition. (c–e) The model with the additional spinel to perovskite transition. Plate c) shows the mass flux at the $\alpha - \beta$ transition for that model, plate d) the mass flux at the $\beta - \gamma$ transition, and plate e) the mass flux at the spinel to perovskite transition. The radial distance to the various phase transitions are as in Fig. 18

located 170 km above the core–mantle boundary together with the two exothermic phase transitions discussed above.

Similar to the models lacking a perovskite layer, a reduction of the number of upwelling plumes can be observed (Fig. 18c,d). One reason is that small scale disturbances are suppressed by the perovskite layer while long wavelength perturbations become stable and result in a few upwellings that arise from below the phase boundary. However, there are also several smaller instabilities that arise from above the endothermic phase boundary. Both types of plumes merge as in the case without perovskite layer to generate a small number of relatively large upwellings. The instabilities originating above the endothermic phase boundary have been underestimated
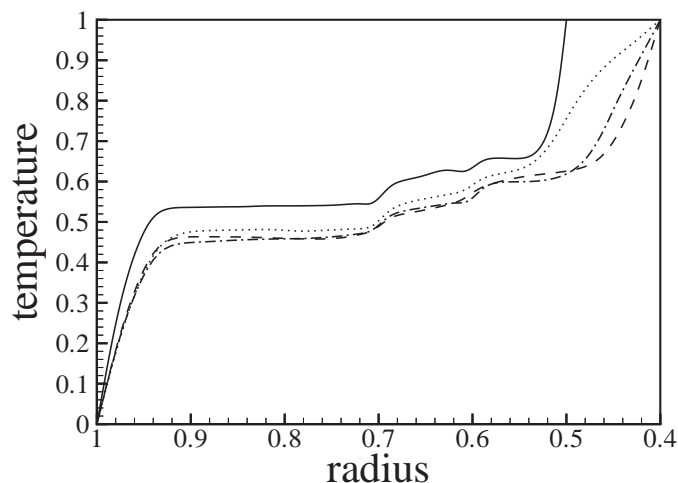
Fig. 22. Temperature profile for the model with two exothermic phase transitions (solid line) and for the model with the spinel–perovskite transition at varying depth and both exothermic phase transitions. The dotted line corresponds to $r_{sp/per} = 0.5 \times r_p$, the dash-dotted line to $r_{sp/per} = 0.45 \times r_p$, and the dashed line to $r_{sp/per} = 0.425 \times r_p$

in the 2D calculations by Weinstein (1995) and in the 3D calculations by Harder and Christensen (1996) and Harder (1997) in which latent heat release and consumption and adiabatic cooling have been neglected. Neglecting these processes also results in much hotter and stronger upwellings as compared to the plumes shown here.

In addition, mantle and plume temperatures, flow velocities, and the time dependence of vertical mass flux are significantly influenced by the presence of the perovskite layer. The spinel-perovskite transition near the core–mantle boundary causes the material near the core to stagnate and thickens the lower thermal boundary (Fig. 21b). This isolating effect results in a lower heat flow from the core and, therefore, in higher temperatures at the core–mantle boundary and the deep mantle as compared to the model without spinel to peroskite transition (Fig. 22). Upwellings reaching the base of the lithosphere are weaker for the model with spinel to perovskite transition; the plume excess temperature is a few tens K lower. Further, as compared to the model without spinel-perovskite transition there is a lower oscillation rate of the vertical mass flux and the mean mantle flow is 0.5 to 4 times slower depending on the perovskite layer thickness. The variation of the perovskite layer thickness (Breuer et al. 1997b) shows that with decreasing perovskite layer thickness, the leaking to the mantle above, the thickening of the thermal boundary layer, and the mantle velocities decrease.

The effects of the phase transitions on mantle dynamics discussed above suggest that the assumptions on which previous thermal evolution models with simple parameterized convection schemes are based may be overly simplistic. Because of the uncertainty in the early core size and the early mantle temperatures at least three evolution scenarios seem to be possible and will be discussed in the following. For these scenarios we assume the present core size to be between 1600 and 1700 km as suggested by the interior structure models in this paper. The scenarios differ mainly in the presence of the spinel-perovskite transitions. The two major exothermic phase

transitions (α-to-β-spinel and β-to-γ-spinel) are present in the Martian mantle during the whole evolution.

The basic assumption of the first scenario is that a perovskite layer is absent or too thin (a few tens of km) to significantly influence the convection flow and that temperatures in the deep mantle have always been lower than about 2100 K. The latter assumption merits a further comment. It is conceivable that the mantle temperature was effectively limited to be not much in excess of the solidus of the Martian mantle. Significantly larger temperatures suggest melt fractions that would effectively be removed due to their inherent buoyancy. For shallow depths this melt would rise to the surface. Because melt is much more compressive than solid rock there is a crossover pressure beyond which melt is denser than rock and would sink to the bottom of the mantle (Stolper et al. 1981) where it would possibly recrystallize. For the pressure range of the deep Martian mantle the solidus temperature is around 2300 K for dry terrestrial peridotite (Takahashi 1990). But we have to consider that the higher iron content will reduce the melting temperature by a few 100 K.

The thermal evolution in this case would be modified by the effects of the exothermic phase transitions on the flow. Latent heat release would result in a temperature increase of about 50 K at each transition (Fig. 22). Therefore, temperatures in the lower mantle may be around 100 K higher than in simple thermal models that neglect phase transitions. In addition, the periodic change of flow blockage and flow acceleration at the phase boundaries would result in a slower cooling and the present temperatures could be even higher. A strong time dependent volcanic activity is also expected as a result of flow blocking and acceleration.

The time dependence of mantle flow induced by the phase transitions could have some important implications for the evolution of the core and the dynamo. The core to mantle heat flow will fluctuate in response to the flow variations. While the core would cool in the long term average, it is conceivable that the temperature gradient near the core–mantle boundary could alternate between subadiabatic and superadiabatic for some time. This would force the heat transfer to alternate between conductive and convective and may switch the dynamo on and off. There are no observational data that would support or require such a scenario and the heat flow variations in Breuer et al. (1997b) are within a few tens of percent of the average value. Judging from the models of Schubert and Spohn (1990) this is not expected to affect the history of the dynamo very much except perhaps for the time when the heat flow from the core drops below the threshold of the heat flow conducted down the core adiabat. However, it should be noted that the parameterized thermal evolution model assumes constant values of temperature and heat flow at the core–mantle boundary. The more realistic convection models suggest that there may be lateral variations in these quantities induced by the mantle temperature distribution. These lateral variations may induce core convection even when the average vertical temperature gradient is conductive. While we do not believe that this will severely alter the conclusions reached by Schubert and Spohn (1990), it is possible that the lifetime of the dynamo will be increased to some extent. The data from the Shergotty meteorite (Cisowski 1986) suggests that Mars may have had a magnetic field with a dipole moment of 10^{13} T m^3 only 1.3 Ga ago. It should be noted that the temperature increases across the phase transitions translate into elevated core temperatures. These results therefore increase the likelihood of the core to remain entirely molten up to the present time.

The basic assumption of the second scenario is that a few 100 km thick perovskite layer is present during the whole evolution. The presence of a perovskite layer sufficiently thick to affect the convection flow field significantly during the

whole evolution implies temperatures in the deep mantle to have always been in excess of about 2100 K. The thermal evolution for this model would be characterized by a slowly changing temperature of the deep mantle which would be due to the strong isolating effect of the perovskite layer. The planet would be cooling from above in producing a thick lithosphere and the mean Rayleigh number would decrease slowly due to the increasing lithosphere thickness. As in the previous scenario, a strong time dependence in the volcanic activity due the combined action of the phase transitions would be likely. This scenario would have even larger core temperatures as compared with the previous one. It is likely, however, due to the reduced rates of heat transfer through the perovskite layer, that the core dynamo would be shut down relatively early, a feature apparently in conflict with the remnant magnetization of the Shergotty meteorites.

The basic assumption of the third scenario is that a few 100 km thick perovskite layer existed during the early evolution but disappeared later either due to cooling of the deep mantle or due to some secular growth of the core. For both cases the thickness of the perovskite layer would decrease with time. With a decreasing thickness of the perovskite layer, the mean mantle velocity, the frequence of vertical mass flux at the exothermic phase transitions, and the plume excess temperatures would also decrease (Breuer et al. 1997b). When the perovskite layer becomes thinner than a few tens of km its effect on the flow would become negligible. At that point in time an increase in volcanic activity could result as the mantle flow velocity and the excess temperature of the upwellings would increase. A peak of volcanic activity has been suggested by Tanaka et al. (1992) to have occurred 3.5 or 4 Ga ago depending on the crater statistic model. The subsequent evolution would be similar to that of the first scenario.

With our present knowledge of Mars it is difficult to decide which of these evolution scenarios is most realistic. However, the inclusion of the phase transitions in mantle convection models makes us aware that the dynamics of the Martian mantle and the thermal evolution of the planet may be more complicated and richer in features than thought before. Common to all of the three models is the time dependence and the partial layering of the mantle flow. This result can explain time dependent rates of volcanic activity and results in a slower and less uniform cooling of the planet as compared to the parameterized evolution models. The present mantle temperatures, in particular those in the deep mantle, should be higher than predicted by previous thermal evolution models. Higher temperatures in the deep mantle suggest higher temperatures in the core and the latter is even more likely to be entirely molten. It should be noted that the elevated temperatures in the deep mantle may help explain the small tidal Q values. Dissipation of tidal energy would occur mostly in the deep mantle near the core–mantle boundary. A layer of relatively hot mantle reduced in viscosity could allow a significant amount of dissipation of tidal energy.

4. Outlook

We have reviewed our present kwowledge of Mars at the eve of a conserted effort to explore the red planet by spacecraft. At the time of this writing *Mars Global Surveyor* and *Mars Pathfinder* are on their way to the planet. These missions are the first in a series of NASA missions in the framework of the Surveyor programme that may end with a sample return mission. Unfortunately, the Russian *Mars96* mission failed in November 1996 but European scientists are working hard to get a replacement mission. Among other important measurements, this mission would have provided us

with a global digital terrain model of unprecedented accuracy and with seismic data. Whether or not seismology will be done on Mars in the forseeable future is unclear at this point. The International Mars Working Group, a working group consisting of representatives of the space agencies has recommended a seismic network as the next logical step in the exploration of Mars. Unfortunately, two attempts at an European led network mission to Mars have not made it beyond phase A. The success of seismology in Geophysics proves that this method provides the best means of studying the interior structure of a planetary body. Nevertheless, even if we will not see a seismic network on Mars in the near future, the missions ahead will immensely improve our understanding of the structure and evolution of the planet. We will probably be able to settle the question about the principal polar moment of inertia factor through a determination of the precession rate of the Martian rotation axis by two-way X-Band Doppler tracking of the *Mars Pathfinder* landing site. The experiment will further improve our knowledge of the rotation rate and state of the planet. The improved knowledge of the moment of inertia factor will enable us to determine the core radius and the Fe/Si ratio with reasonable accuracy although a final answer would still require a seismic measurement of the core radius. We will also be able to better constrain the existence of the deep mantle phase transitions. However, what has been said about the core radius applies here even more. The existence of mantle phase transitions cannot be unambigously determined from gravity and rotation data. The Atmospheric Structure Instrument on *Mars Pathfinder* will measure the temperature and density of the atmosphere during descent. The mission includes a small tethered rover that carries an α-proton X-ray spectrometer to measure the major element composition of Martian rock. The minirover will move to a rock of interest within a distance of a few tens of meter from the spacecraft to do the measurement. A camera on the lander equipped with an infrared filter will image the immediate surroundings of the lander and do some infrared spectroscopy.

The radar altimetry experiment on *Mars Global Surveyor* will yield the topography to an accuracy of better than 100 m. The camera on the orbiter will produce weather photographs but by using the narrow angle lens can capture images of objects as small as 1.5 m. A magnetometer will measure the magnetic field and may be able to detect magnetic field anomalies due to remnantly magnetized rock. A thermal emission spectrometer will be used to map the the mineral composition of the surface and to study temperature induced atmosphere-surface interactions.

The Japanese orbiter mission *Planet B* is intended to be launched in summer 1998 and will begin studying near-Mars space in autumn 1999. The nominal mission duration is one Martian year. The instruments on the spacecraft will be used to determine the structure and composition of the Martian ionosphere and its interaction with the solar wind and the interplanetary magnetic field. The atmospheric ratio of hydrogen to deuterium will be measured with high accuracy which is essential to understand the possible early escape of water from the planet's surface. The camera on *Planet B* will monitor the global seasonal weather activity on Mars in terms of large-scale dust storm occurences and variable distributions of clouds and hazes in the lower atmosphere. The camera will also take some close-up images when the spacecraft encounters close passages of Phobos and Deimos. Furthermore, instruments on *Planet B* will be used to search for possible dust rings around Mars which may have formed due to impacts of meteoroids into the regolith layers of the Martian satellites.

Although these missions will greatly improve our knowledge of Mars some burning questions remain. Among these questions is that to the state of the core. Is it solid

or liquid or liquid with a solid inner core. An answer to that question will provide important constraints for models of interior structure and evolution as our review should have indicated. The state of the core can only be resolved by seismology. Of similar importance, of course, would be a sample or samples returned from the Martian surface. Analysis of these would remove or confirm some doubts about the origin of the SNC meteorites among scientists. If all goes well within the next decade, these questions and many more posed by experts in meteorology, atmosphere science, life science, geology, and cosmochemistry will be answered. It is conceivable that we will soon know Mars better than we know the Moon even without manned space exploration. Our knowledge of Mars will not only serve planetology but also allow us to further our understanding of our home planet, the Earth, by having a similarly well known but interestingly enough different planet to compare with.

References

Anderson, D. L. (1972). Internal constitution of Mars. *J. Geophys. Res.*, **77**, 789–795.

Ash, R. D., Knott, S. F., and Turner, G. (1996). A 4-Gyr shock age for a martian meteorite and implications for the cratering history of Mars. *Nature*, **380**, 57–59.

Avanesov, G. A., Bonev, B. I., Kempe, F., Basilevsky, A. T., Boycheva, V., Chikov, K. N., Danz, M., Dimitrov, D., Duxbury, T., Gromatikov, P., Halmann, D., Head, J., Heifets, V. N., Kolev, V., Kostenko, V. I., Kottsov, V. A., Krasavtsev, V. M., Krasikov, V. A., Krumov, A., Kuzmin, A. A., Losev, K. D., Lumme, K., Mishev, D. N., Möhlmann, D., Muinonen, K., Murav'ev, V. M., Murchie, S., Murray, B., Neumann, W., Paul, L., Petkov, D., Petuchova, I., Pössel, W., Redel, B., Shkuratov, Y. G., Simeonov, S., Smith, B., Totev, A., Uzunov, Y., Fedotov, V. P., Weide, G.-G., Zapfe, H., Zhukov, B. S., and Ziman, Y. L. (1989). Television observations of Phobos. *Nature*, **341**, 585–587.

Baker, V. R., Strom, R. G., Croft, S. K., Gullick, V. C., Kargel, J. S., and Komatsu, G. (1991). Ancient oceans, ice sheets and the hydrological cycle on Mars. *Nature*, **352**, 589–594.

Baker, V. R., Carr, M. H., Gulick, V. C., Williams, C. R., and Marley, M. S. (1992). Channels and valley networks. In H. H. Kieffer, B. M. Jakosky, C. W. Snyder, and M. S. Matthews, editors, *Mars*, pages 453–492. Univ. of Ariz. Press, Tucson.

Balmino, G., Moynot, G., and Valés, N. (1982). Gravity field model of Mars in spherical harmonics up to degree and order eighteen. *J. Geophys. Res.*, **87**, 9735–9746.

Banerdt, W. B., Phillips, R. J., Sleep, N. H., and Saunders, R. S. (1982). Thick shell tectonics on one-plate planets: Applications to Mars. *J. Geophys. Res.*, **87**, 9723–9733.

Banerdt, W. B., Golombek, M. P., and Tanaka, K. L. (1992). Stress and tectonics on Mars. In H. H. Kieffer, B. M. Jakosky, C. W. Snyder, and M. S. Matthews, editors, *Mars*, pages 249–297. Univ. of Ariz. Press, Tucson.

Banerdt, W. B., Chicarro, A. F., Coradini, M., Federico, C., Greeley, R., Hechler, M., Knudsen, J. M., Leovy, C., Lognonné, P., Lowry, L., McCleese, D., McKay, C., Pellinen, R., Phillips, R., Scoon, G. E. N., Spohn, T., Squyres, S., Taylor, F., and Wänke, H. (1996). *INTERMARSNET Phase-A Study Report*. European Space Agency, ESTEC, Paris. esa SCI(96)2.

Banin, A., Clark, B. C., and Wänke, H. (1992). Surface chemistry and mineralogy. In H. H. Kieffer, B. M. Jakosky, C. W. Snyder, and M. S. Matthews, editors, *Mars*, pages 594–625. Univ. of Ariz. Press, Tucson.

Basaltic Volcanism Study Project (1981). *Basaltic Volcanism on the Terrestrial Planets*. Pergamon Press, New York.

Batson, R. M., Edwards, K., and Duxbury, T. C. (1992). Geodesy and cartography of the Martian satellites. In H. H. Kieffer, B. M. Jakosky, C. W. Snyder, and M. S. Matthews, editors, *Mars*, pages 1249–1256. Univ. of Ariz. Press, Tucson.

Bertka, C. M. and Fei, Y. (1996). Constraints on the mineralogy of an iron-rich Martian mantle from high-pressure experiments. *Planet. Space Sci.*, **44**, 1269–1276.

Bertka, C. M. and Fei, Y. (1997). Mineralogy of the Martian interior up to core-mantle boundary pressures. *J. Geophys. Res.*, **102**, 5251–5264.

Bills, B. G. (1989). The moments of inertia of Mars. *Geophys. Res. Lett.*, **16**, 385–388.

Bills, B. G. and Ferrari, A. J. (1978). Mars topography harmonics and geophysical implications. *J. Geophys. Res.*, **83**, 3497–3508.

Binder, A. B. (1969). Internal structure of Mars. *Phys. Earth Planet. Inter.*, **74**, 3110–3118.

Binder, A. B. and Davis, D. R. (1973). Internal structure of Mars. *Phys. Earth Planet. Inter.*, **7**, 477–485.

Born, G. H. (1974). Mars physical parameters as determined from Mariner 9 observations of the natural satellites and Doppler tracking. *J. Geophys. Res.*, **79**, 4837–4844.

Breuer, D., Spohn, T., and Wüllner, U. (1993). Mantle differentiation and the crustal dichotomy of Mars. *Planet. Space Sci.*, **41**, 269–283.

Breuer, D., Zhou, H., Yuen, D. A., and Spohn, T. (1996). Phase transitions in the Martian mantle: Implications for the planet's volcanic history. *J. Geophys. Res.*, **101**, 7531–7542.

Breuer, D., Yuen, D. A., Spohn, T., and Zhang, S. (1997a). Three dimensional models of Martian mantle convection with phase transitions. *Geophys. Res. Lett.*, **25**, 229–232.

Breuer, D., Yuen, D. A., and Spohn, T. (1997b). Phase transitions in the Martian mantle: Implications for partially layered convection. *Earth Planet. Sci. Lett.*, **148**, 457–469.

Burns, J. A. (1986). The evolution of satellite orbits. In J. A. Burns and M. S. Matthews, editors, *Satellites*, pages 117–158. Univ. of Ariz. Press, Tucson.

Burns, J. A. (1992). Contradictory clues as to the origin of the Martian moons. In H. H. Kieffer, B. M. Jakosky, C. W. Snyder, and M. S. Matthews, editors, *Mars*, pages 1283–1301. Univ. of Ariz. Press, Tucson.

Carr, M. H. (1981). *The Surface of Mars*. Yale Univ. Press, New Haven.

Carr, M. H. (1986). Mars: A water–rich planet? *Icarus*, **68**, 187–216.

Carr, M. H., Crumpler, L. S., Cutts, J. A., Greeley, R., Guest, J. E., and Masursky, H. (1977). Martian impact craters. *J. Geophys. Res.*, **82**, 4055–4065.

Chen, J. H. and Wasserburg, G. J. (1986). Formation ages and evolution of Shergotty and its parent planet from U-Th-Pb systematics. *Geochim. Cosmochim. Acta*, **50**, 955–968.

Chicarro, A. F., Coradini, M., Fulchignoni, M., Hiller, K., Knudsen, J. M., Liede, I., Lindberg, C., Lognonné, P., Pellinen, R., Spohn, T., Scoon, G. E. N., Taylor, F., and Wänke, H. (1993). *MARSNET Phase-A Study Report*. European Space Agency, ESTEC, Paris. esa SCI(93)2.

Chopelas, A., Boehler, R., and Ko, T. (1994). Thermodynamics and behavior of γ-Mg_2SiO_4 at high pressure: Implications for Mg_2SiO_4 phase equilibrium. *Phys. Chem. Min.*, **21**, 351–359.

Christensen, E. J. (1975). Martian topography derived from occultation, radar, spectral, and optical measurements. *J. Geophys. Res.*, **80**, 2909–2913.

Christensen, E. J. and Balmino, G. (1979). Development and analysis of a twelfth degree and order gravity model of Mars. *J. Geophys. Res.*, **84**, 7943–7953.

Christensen, U. R. and Yuen, D. A. (1985). Layered convection induced by phase transitions. *J. Geophys. Res.*, **90**, 10291–10300.

Cisowski, S. M. (1986). Magnetic studies on Shergotty and other SNC meteorites. *Geochim. Cosmochim. Acta*, **50**, 1043–1048.

Clark, R. N., Fanale, F. P., and Gaffey, M. J. (1986). Surface composition of natural satellites. In J. A. Burns and M. S. Matthews, editors, *Satellites*, pages 437–491. Univ. of Ariz. Press, Tucson.

Comer, R. P., Solomon, S. C., and Head, J. W. (1985). Mars: Thickness of the lithosphere from the tectonic response to volcanic loads. *Rev. Geophys.*, **23**, 61–92.

Connerney, J. E. P. (1993). Magnetic fields of the outer planets. *J. Geophys. Res.*, **98**, 18659–18679.

Cook, A. H. (1977). The moment of inertia of Mars and the existence of a core. *Geophys. J. R. Astron. Soc.*, **51**, 349–356.

Davies, M. E., Batson, R. M., and Wu, S. S. C. (1992). Geodesy and cartography. In H. H. Kieffer, B. M. Jakosky, C. W. Snyder, and M. S. Matthews, editors, *Mars*, pages 321–342. Univ. of Ariz. Press, Tucson.

Dreibus, G. and Wänke, H. (1985). Mars: A volatile rich planet. *Meteoritics*, **20**, 367–382.

Dreibus, G. and Wänke, H. (1987). Volatiles on Earth and Mars: A comparison. *Icarus*, **71**, 225–240.

Esposito, P. B., Banerdt, W. B., Lindal, G. F., Sjogren, W. L., Slade, M. A., Bills, B. G., Smith, D. E., and Balmino, G. (1992). Gravity and topography. In H. H. Kieffer, B. M. Jakosky, C. W. Snyder, and M. S. Matthews, editors, *Mars*, pages 209–248. Univ. of Ariz. Press, Tucson.

Fei, Y., Prewitt, C. T., Mao, H. K., and Bertka, C. M. (1995). Structure and density of FeS at high pressure and high temperature and the internal structure of Mars. *Science*, **268**, 1892–1894.

Frey, H. V., Semeniuk, A. M., Semeniuk, J. A., and Tokarcik, S. (1988). A widespread common age resurfacing event in the highland-lowland transition zone in eastern Mars. In *Proceedings of the 18th Lunar Planet. Sci. Conf.*, pages 679–699. Lunar and Planetary Science Institute.

Göttel, K. A. (1981). Density of the mantle of Mars. *Geophys. Res. Lett.*, **8**, 497–500.

Grady, M. M., Wright, I. P., and Pillinger, C. T. (1996). Opening a martian can of worms? *Nature*, **382**, 575–576.

Greeley, R. and Spudis, P. D. (1981). Volcanism on Mars. *Rev. Geophys.*, **19**, 13–41.

Harder, H. (1997). Phase transitions and the 3D-planform of thermal convection in the Martian mantle. *J. Geophys. Res.*, in press.

Harder, H. and Christensen, U. R. (1996). A one-plume model of martian mantle convection. *Nature*, **380**, 507–509.

Hartmann, W. K., Strom, R. G., Weidenschilling, S. J., Blasius, K. R., Woronow, A., Grieve, M. R., Diaz, R. A. F., Chapman, C. R., Shoemaker, E. N., and Jones, K. L. (1981). Chronology of planetary volcanism by comparative studies of planetary cratering. In *Basaltic Volcanism on the Terrestrial Planets*, pages 1049–1127. Pergamon Press, New York.

Jagoutz, E. (1991). Chronology of SNC meteorites. *Space Sci. Rev.*, **56**, 13–22.

Janle, P. (1983). Bouguer gravity profiles across the highland–lowland escarpment on Mars. *Earth Moon Planets*, **28**, 55–67.

Janle, P. and Jannsen, D. (1986). Isostatic gravity and elastic bending models of Olympus Mons, Mars. *Ann. Geophys.*, **4**, 537–546.

Janle, P. and Meissner, R. (1986). Structure and evolution of the terrestrial planets. *Surv. Geophys.*, **8**, 107–186.

Johnston, D. H. and Toksöz, M. N. (1977). Internal structure and properties of Mars. *Icarus*, **32**, 73–84.

Johnston, D. H., McGetchin, T. R., and Toksöz, M. N. (1974). The thermal state and internal structure of Mars. *J. Geophys. Res.*, **79**, 3959–3971.

Kamaya, N., Ohtani, E., Kato, T., and Onuma, K. (1993). High pressure phase transitions in a homogeneous model Martian mantle. In E. Takahashi, R. Jeanloz, and D. Rubie, editors, *Evolution of the Earth and Planets*, volume 74 of *Geophys. Monogr. Ser.*, pages 19–25. AGU, Washington, D.C.

Kaula, W. M. (1968). *An Introduction to Planetary Physics: The Terrestrial Planets*. John Wiley, New York.

Kaula, W. M. (1979). The moment of inertia of Mars. *Geophys. Res. Lett.*, **6**, 194–196.

Kiefer, W. S., Bills, B. G., Nerem, R. S., and Zuber, M. T. (1996). An inversion of gravity and topography for mantle and crustal structure on Mars. *J. Geophys. Res.*, **101**, 9239–9252.

Kieffer, H. H., Jakosky, B. M., and Snyder, C. W. (1992). The planet Mars: From antiquity to the present. In H. H. Kieffer, B. M. Jakosky, C. W. Snyder, and M. S. Matthews, editors, *Mars*, pages 1–33. Univ. of Ariz. Press, Tucson.

Kivelson, M. G., Khurana, K. K., Walker, R. J., Warnecke, J., Russell, C. T., Linker, J. A., Southwood, D. J., and Polanskey, C. (1996a). Io's interaction with the plasma torus: Galileo magnetometer report. *Science*, **274**, 396–398.

Kivelson, M. G., Khurana, K. K., Walker, R. J., Russell, C. T., Linker, J. A., Southwood, D. J., and Polanskey, C. (1996b). A magnetic signature at Io: initial report from the Galileo magnetometer. *Science*, **273**, 337–340.

Ksanfomality, L. V., Moroz, V. I., Bibring, J. P., Combes, M., Soufflot, A., Ganpantzerova, O. F., Goroshkova, N. V., Zharkov, A. V., and Nikitin, G. E. (1989). Spatial variations in thermal and albedo properties of the surface of Phobos. *Nature*, **341**, 588–591.

Leliwa-Kopystyński, J. and Bakun-Czubarow, N. (1980). The effect of material parameters on the shape of the phase separation surfaces within the Earth's mantle. *Phys. Earth Planet. Inter.*, **22**, 244–254.

Leweling, M. and Spohn, T. (1997). Mars: a magnetic field due to remanence? *Planet. Space Sci.*, **45**, 1389–1400.

Lognonné, P. and Mosser, B. (1993). Planetary seismology. *Surv. Geophys.*, **14**, 239–302.

Longhi, J., Knittle, E., Holloway, J. R., and Wänke, H. (1992). The bulk composition, mineralogy and internal structure of Mars. In H. H. Kieffer, B. M. Jakosky, C. W. Snyder, and M. S. Matthews, editors, *Mars*, pages 184–208. Univ. of Ariz. Press, Tucson.

Lucchitta, B. K. (1987). Recent mafic volcanism on Mars. *Science*, **235**, 565–567.

Lucchitta, B. K., McEwen, A. S., Clow, G. D., Geissler, P. E., Singer, R. B., Schultz, R. A., and Squyres, S. W. (1992). The canyon system on Mars. In H. H. Kieffer, B. M. Jakosky, C. W. Snyder, and M. S. Matthews, editors, *Mars*, pages 453–492. Univ. of Ariz. Press, Tucson.

Luhmann, J. G. and Brace, L. H. (1991). Near-Mars space. *Rev. Geophys.*, **29**, 121–140.

Luhmann, J. G., Russell, C. T., Brace, L. H., and Vaisberg, O. L. (1992). The intrinsic magnetic field and solar-wind interaction of Mars. In H. H. Kieffer, B. M. Jakosky, C. W. Snyder, and M. S. Matthews, editors, *Mars*, pages 1090–1134. Univ. of Ariz. Press, Tucson.

Machetel, P. and Yuen, D. A. (1988). Infinite Prandtl number spherical-shell convection. In N. J. Vlaar, S. Cloetingh, and R. Wortel, editors, *Mathematical Geophysics*, pages 265–290. D. Reidel.

Matyska, C., Yuen, D. A., and Breuer, D. (1996). Symmetries of volcanic distributions on Mars and its internal dynamics. UMSI96/226, Minneapolis.

McCauley, J. F., Carr, M. H., Cutts, J. A., Hartmann, W. K., Masursky, H., Milton, D. J., Sharp, R. P., and Wilhelms, D. E. (1972). Preliminary Mariner 9 report on the geology of Mars. *Icarus*, **17**, 289–327.

McGetchin, T. R. and Smyth, J. R. (1978). The mantle of Mars: Some possible geological implications of its high density. *Icarus*, **34**, 512–536.

McGill, G. E. and Dimitriou, A. M. (1990). Origin of the Martian global dichotomy by crustal thinning in the late Noachian or early Hesperian. *J. Geophys. Res.*, **95**, 12,595–12,605.

McKay, D. S., Gibson Jr., E. K., Thomas-Keprta, K. L., Vali, H., Romanek, C. S., Clemett, S. J., Chillier, X. D. F., Maechling, C. R., and Zare, R. N. (1996). Search for past life on Mars: Possible relic biogenic activity in Martian meteorite ALH84001. *Science*, **273**, 924–930.

McSween, H. Y. (1985). SNC meteorites: Clues to Martian petrologic evolution? *Rev. Geophys.*, **23**, 391–416.

McSween, H. Y. (1987). *Meteorites and their parent planets*. Cambridge Univ. Press, Cambridge.

Meissner, R. O. (1986). *The Continental Crust: A Geophysical Approach*. Academic Press, Orlando.

Mittlefehldt, D. W. (1994). ALH84001, a cumulate orthopyroxenite member of the martian meteorite clan. *Meteoritics*, **29**, 214–221.

Mocquet, A., Vacher, P., Grasset, O., and Sotin, C. (1996). Theoretical seismic models of Mars: the importance of the iron content of the mantle. *Planet. Space Sci.*, **44**, 1251–1268.

Morgan, J. W. and Anders, E. (1979). Chemical composition of Mars. *Geochim. Cosmochim. Acta*, **43**, 1601–1610.

Mouginis-Mark, P. J., McCoy, T. J., Taylor, G. J., and Keil, K. (1992). Martian parent craters for the SNC meteorites. *J. Geophys. Res.*, **97**, 10,213–10,225.

Neukum, G. and Hiller, K. (1981). Martian ages. *J. Geophys. Res.*, **86**, 3097–3121.

Neukum, G. and Wise, D. U. (1976). Mars: A standard crater curve and possible new time scale. *Science*, **194**, 1381–1387.

Ohtani, E. and Kamaya, N. (1992). The geochemical model of Mars: An estimation from the high pressure experiments. *Geophys. Res. Lett.*, **19**, 2239–2242.

Okal, E. A. and Anderson, D. L. (1978). Theoretical models for Mars and their seismic properties. *Icarus*, **33**, 514–528.

Owen, T. (1992). The composition and early history of the atmosphere of Mars. In H. H. Kieffer, B. M. Jakosky, C. W. Snyder, and M. S. Matthews, editors, *Mars*, pages 818–834. Univ. Arizona Press, Tucson.

Phillips, R. J. and Lambeck, K. (1980). Gravity fields of the terrestrial planets: Long–wavelength anomalies and tectonics. *Rev. Geophys.*, **18**, 27–76.

Phillips, R. J. and Saunders, R. S. (1975). The isostatic state of Martian topography. *J. Geophys. Res.*, **80**, 2893–2898.

Pollack, J. B., Kasting, J. F., Richardson, S. M., and Poliakoff, K. (1987). The case for a wet, warm climate on early Mars. *Icarus*, **71**, 203–224.

Reasenberg, R. D. (1977). The moment of inertia and isostasy of Mars. *J. Geophys. Res.*, **82**, 369–375.

Reasenberg, R. D., Shapiro, I. I., and White, R. D. (1975). The gravity field of Mars. *Geophys. Res. Lett.*, **2**, 89–92.

Riedler, W., Möhlmann, D., Oraevsky, V. N., Schwingenschuh, K., Yeroshenko, Y., Rustenbach, J., Ay-dogar, O., Berghofer, G., Lichtenegger, H., Delva, M., Schelch, G., Pirsch, K., Fremuth, G., Steller, M., Arnold, H., Raditsch, T., Auster, U., Fornacon, K.-H., Schenk, H. J., Michaelis, H., Motschmann, U., Roatsch, T., Sauer, K., Schröter, R., Kurths, J., Lenners, D., Linthe, J., Kobzev, V., Styashkin, V., Achache, J., Slavin, J., Luhmann, J. G., and Russell, C. T. (1989). Magnetic fields near Mars: first results. *Nature*, **341**, 604–607.

Ringwood, A. E. (1979). *On the Origin of the Earth and Moon*. Springer-Verlag, New York.

Russell, C. T. (1993). Magnetic fields of the terrestrial planets. *J. Geophys. Res.*, **98**, 18,681–18,695.

Russell, C. T., Luhmann, J. G., Spreiter, J. R., and Stahara, S. S. (1984). The magnetic field of Mars: Implications from gas dynamic modeling. *J. Geophys. Res.*, **89**, 2997–3003.

Schubert, G. and Spohn, T. (1990). Thermal history of Mars and the sulfur content of its core. *J. Geophys. Res.*, **95**, 14,095–14,104.

Schubert, G., Solomon, S. C., Turcotte, D. L., Drake, M. J., and Sleep, N. H. (1992). Origin and thermal evolution of Mars. In H. H. Kieffer, B. M. Jakosky, C. W. Snyder, and M. S. Matthews, editors, *Mars*, pages 147–183. Univ. of Ariz. Press, Tucson.

Schultz, P. H. (1986). Crater ejecta morphology and the presence of water on Mars. In *Symposium on Mars: Evolution of its climate and atmosphere*, pages 95–97. Lunar and Planetary Institute, Houston.

Schultz, P. H. and Gault, D. E. (1979). Atmospheric effects on Martian ejecta emplacement. *J. Geophys. Res.*, **84**, 7669–7687.

Sharp, R. P. (1973). Mars: Fretted and chaotic terrain. *J. Geophys. Res.*, **78**, 4073–4083.

Singer, R. B. and McSween, Jr., H. Y. (1993). The igneous crust of Mars: Compositional evidence from remote sensing and the SNC meteorites. In J. Lewis, M. S. Matthews, and M. L. Guerrieri, editors, *Resources of Near-Earth Space*, pages 709–736. Univ. of Ariz. Press, Tucson.

Sjogren, W. L., Lorell, J., Wong, L., and Downs, W. (1975). Mars gravity field based on a short arc technique. *J. Geophys. Res.*, **80**, 2899–2908.

Sleep, N. H. (1994). Martian plate tectonics. *J. Geophys. Res.*, **99**, 5639–5655.

Smith, D. E. and Zuber, M. T. (1996). The shape of Mars and the topographic signature of the hemispheric dichotomy. *Science*, **271**, 184–187.

Smith, D. E., Lerch, F. J., Nerem, R. S., Zuber, M. T., Patel, G. B., Fricke, S. K., and Lemoine, F. G. (1993). An improved gravity model for Mars: Goddard Mars Model 1. *J. Geophys. Res.*, **98**, 314–324.

Smith, J. C. and Born, G. H. (1976). Secular acceleration of Phobos and Q of Mars. *Icarus*, **27**, 51–53.

Soderblom, L. A. (1992). The composition and mineralogy of the Martian surface from spectroscopic observations: 0.3 μm to 50 μm. In H. H. Kieffer, B. M. Jakosky, C. W. Snyder, and M. S. Matthews, editors, *Mars*, pages 557–593. Univ. of Ariz. Press, Tucson.

Sohl, F. and Spohn, T. (1997). The interior structure of Mars: Implications from SNC meteorites. *J. Geophys. Res.*, **102**, 1613–1635.

Solomon, S. C. (1979). Formation, history, and energetics of cores in the terrestrial planets. *Phys. Earth Planet. Inter.*, **19**, 168–182.

Solomon, S. C. and Head, J. W. (1982). Evolution of the Tharsis province of Mars: The importance of heterogeneous lithospheric thickness and volcanic construction. *J. Geophys. Res.*, **87**, 9755–9774.

Spohn, T. (1991). Mantle differentiation and thermal evolution of Mars, Mercury, and Venus. *Icarus*, **90**, 222–236.

Squyres, S. W., Clifford, S. M., Kuzmin, R. O., Zimbelman, J. R., and Costard, F. M. (1992). Ice in the Martian regolith. In H. H. Kieffer, B. M. Jakosky, C. W. Snyder, and M. S. Matthews, editors, *Mars*, pages 523–556. Univ. of Ariz. Press, Tucson.

Stacey, F. D., Brennan, B. J., and Irvine, R. D. (1981). Finite strain theories and comparisons with seismological data. *Geophys. Surv.*, **4**, 189–232.

Stevenson, D. J. (1981). Models of the Earth's core. *Science*, **241**, 611–619.

Stevenson, D. J., Spohn, T., and Schubert, G. (1983). Magnetism and thermal evolution of the terrestrial planets. *Icarus*, **54**, 466–489.

Stoker, C. R., Gooding, J. L., Roush, T., Banin, A., Burt, D., Clark, B. C., Flynn, G., and Gwynne, O. (1993). The physical and chemical properties and resource potential of Martian surface soils. In J. Lewis, M. S. Matthews, and M. L. Guerrieri, editors, *Resources of Near-Earth Space*, pages 659–707. Univ. of Ariz. Press, Tucson.

Stolper, E., Walker, D., Hager, B. H., and Hays, J. F. (1981). Melt segregation from partially molten source regions: The importance of melt density and source region size. *J. Geophys. Res.*, **91**, 6261–6271.

Takahashi, E. (1990). Speculations on the Archean mantle: missing link between komatiite and depleted garnet peridotite. *J. Geophys. Res.*, **95**, 15,941–15,954.

Tanaka, K. L. (1986). The stratigraphy of Mars. In *Proceedings of the 17th Lunar and Planetary Sci. Conf.*, volume 91, pages E139–E158. Lunar and Planetary Science Institute, Houston.

Tanaka, K. L., Scott, D. H., and Greeley, R. (1992). Global stratigraphy. In H. H. Kieffer, B. M. Jakosky, C. W. Snyder, and M. S. Matthews, editors, *Mars*, pages 345–382. Univ. of Ariz. Press, Tucson.

Taylor, S. R. (1988). Planetary compositions. In J. F. Kerridge and M. S. Matthews, editors, *Meteorites and the Solar System*, pages 512–534. Univ. of Ariz. Press, Tucson.

Taylor, S. R. (1992). *Solar System Evolution: A New Perspective*. Cambridge Univ. Press, Cambridge.

Thomas, P., Veverka, J., and Dermott, S. (1986). Small satellites. In J. A. Burns and M. S. Matthews, editors, *Satellites*, pages 802–835. Univ. of Ariz. Press, Tucson.

Thomas, P., Veverka, J., Bell, J., Lunine, J., and Cruikshank, D. (1992). Satellites of Mars: Geologic history. In H. H. Kieffer, B. M. Jakosky, C. W. Snyder, and M. S. Matthews, editors, *Mars*, pages 1257–1282. Univ. of Ariz. Press, Tucson.

Thomas, P. C. (1991). Planetary geodesy, U.S. Natl. Rep. Int. Geod. Geophys. 1987–1990. *Rev. Geophys.*, **29**, 182–187.

Thurber, C. H. and Toksöz, M. N. (1978). Martian lithosphere thickness from flexure theory. *Geophys. Res. Lett.*, **5**, 977–980.

Treiman, A. H. (1995). A petrographic history of martian meteorite ALH84001: Two shocks and an ancient age. *Meteoritics*, **30**, 294–302.

Urey, H. C. (1952). *The Planets: Their Origin and Development*. Yale Univ. Press, New Haven, Conn.

Usselman, T. M. (1975). Experimental approach to the state of the core: Part II. Composition and thermal regime. *Amer. J. Sci.*, **275**, 291–303.

Walker, J. C. G. (1978). Atmospheric evolution on the inner planets. In C. Ponnamperuma, editor, *Comparative Planetology*, pages 141–163. Academic Press, New York.

Wänke, H. (1981). Constitution of terrestrial planets. *Philos. Trans. R. Soc. London, Ser. A*, **303**, 287–302.

Wänke, H. (1991). Chemistry, accretion, and evolution of Mars. *Space Sci. Rev.*, **56**, 1–8.

Wänke, H. and Dreibus, G. (1988). Chemical composition and accretion history of terrestrial planets. *Philos. Trans. R. Soc. London, Ser. A*, **325**, 545–557.

Ward, W. R. (1992). Long-term orbital and spin dynamics of Mars. In H. H. Kieffer, B. M. Jakosky, C. W. Snyder, and M. S. Matthews, editors, *Mars*, pages 298–320. Univ. of Ariz. Press, Tucson.

Wasson, J. T. and Kallemeyn, G. W. (1988). Composition of chondrites. *Philos. Trans. R. Soc. London, Ser. A*, **325**, 535–544.

Weinstein, S. A. (1995). The effects of a deep mantle endothermic phase change on the structure of thermal convection in silicate planets. *J. Geophys. Res.*, **100**, 11,719–11,728.

Wells, R. A. (1979). *Geophysics of Mars*. Elsevier, Amsterdam.

Wilhelms, D. E. and Squyres, S. W. (1984). The Martian hemispheric dichtomy may be due to a giant impact. *Nature*, **309**, 138–140.

Willemann, R. J. and Turcotte, D. L. (1982). The role of lithospheric stress in the support of the Tharsis rise. *J. Geophys. Res.*, **87**, 9793–9801.

Wise, D. A., Golombek, M. P., and McGill, G. E. (1979). Tectonic evolution of Mars. *J. Geophys. Res.*, **84**, 7934–7939.

Wright, I. P., Grady, M. M., and Pillinger, C. T. (1989). Organic material in a martian meteorite. *Nature*, **340**, 220–222.

Yoder, C. F. (1982). Tidal rigidity of Phobos. *Icarus*, **49**, 327–346.

Yoder, C. F. and Standish, E. M. (1997). Measurements of the precession and rotation from Viking lander range data. *J. Geophys. Res.*, **102**, 4065–4080.

Zhang, S. and Yuen, D. A. (1996). Various influences on plumes and dynamics in time-dependent, compressible, mantle convection in 3D-spherical shells. *Phys. Earth Planet. Inter.*, **94**, 241–267.

Zharkov, V. N., Koshlyakov, E. M., and Marchenkov, K. I. (1991). The composition, structure, and gravitational field of Mars. *Astron. Vestn.*, **25**(5), 515–547.

Zhou, H., Breuer, D., Yuen, D. A., and Spohn, T. (1995). Phase transitions in the Martian mantle and the generation of megaplumes. *Geophys. Res. Lett.*, **22**, 1945–1948.